ORIGINAL PAPER

Hidden attractors in Chua circuit: mathematical theory meets physical experiments

Nikolay Kuznetsov [iD] · **Timur Mokaev** ·
Vladimir Ponomarenko · **Evgeniy Seleznev** ·
Nataliya Stankevich · **Leon Chua**

Abstract After the discovery in early 1960s by E. Lorenz and Y. Ueda of the first example of a chaotic attractor in numerical simulation of a real physical process, a new scientific direction of analysis of chaotic behavior in dynamical systems arose. Despite the key role of this first discovery, later on a number of works have appeared supposing that chaotic attractors of the considered dynamical models are rather artificial, computer-induced objects, i.e., they are generated not due to the physical nature of the process, but only

†: Evgeniy Seleznev.

N. Kuznetsov
Faculty of Information Technology, University of Jyväskylä, Jyväskylä, Finland

N. Kuznetsov
Institute for Problems in Mechanical Engineering RAS, St. Petersburg, Russia

N. Kuznetsov (✉)· T. Mokaev
Mathematics and Mechanics Faculty, Saint-Petersburg State University, St. Petersburg, Russia
e-mail: nkuznetsov239@gmail.com

V. Ponomarenko · E. Seleznev · N. Stankevich
Kotel'nikov's Institute of Radio-Engineering and Electronics of RAS, Saratov Branch, Saratov, Russia

N. Stankevich
Department of Radio-Electronics and Telecommunication, Yuri Gagarin State Technical University of Saratov, Saratov, Russia
e-mail: stankevichnv@mail.ru

L. Chua
Electrical Engineering Department, University of California, Berkeley, CA, USA

by errors arising from the application of approximate numerical methods and finite-precision computations. Further justification for the possibility of a real existence of chaos in the study of a physical system developed in two directions. Within the first direction, effective analytic-numerical methods were invented providing the so-called computer-assisted proof of the existence of a chaotic attractor. In the framework of the second direction, attempts were made to detect chaotic behavior directly in a physical experiment, by designing a proper experimental setup. The first remarkable result in this direction is the experiment of L. Chua, in which he designed a simple RLC circuit (Chua circuit) containing a nonlinear element (Chua diode), and managed to demonstrate the real evidence of chaotic behavior in this circuit on the screen of oscilloscope. The mathematical model of the Chua circuit (further, Chua system) is also known to be the first example of a system in which the existence of a chaotic hidden attractor was discovered and the bifurcation scenario of its birth was described. Despite the nontriviality of this discovery and cogency of the procedure for hidden attractor localization, the question of detecting this type of attractor in a physical experiment remained open. This article aims to give an exhaustive answer to this question, demonstrating both a detailed formulation of a radiophysical experiment on the localization of a hidden attractor in the Chua circuit, as well as a thorough description of the relationship between a physical experiment, mathematical modeling, and computer simulation.

1 Introduction

The Chua circuit is one of the reference models of non-linear dynamics [1,2]. This model was developed by Leon Chua as the first example of a radiophysical generator where dynamical chaos can be observed in a physical experiment [3]. One of the design goals of this generator was to verify, whether chaotic dynamics exists in reality, or it is the result of computational errors in numerical modeling. In a physical experiment, where the electronic circuit starts with zero initial conditions (initial voltages across the capacitors and the current through the coil), corresponding to the zero equilibrium state, only self-excited attractors could be observed with instability of the zero equilibrium state. Hundreds of such different self-excited attractors have been found in the Chua circuit [4]. Thus, the conjectures were put forward that only self-excited chaotic attractors can exist in the circuit [2] (see also discussions in [5,6]).

In 2009, as a farther development of effective analytical-numerical methods for the study of oscillations [7], the idea of constructing a hidden chaotic Chua attractor was first proposed by Nikolay Kuznetsov [6,8–10] and, in 2011, the first hidden chaotic attractor in the classical Chua circuit [11–13] was discovered. This hidden attractor has a very "thin" basin of attraction, which is not connected with equilibria, and coexists with a stable zero equilibrium, thus being "hidden" for a while for standard physics experiments and mathematical modeling of the circuit with random initial data. In recent years, the discovery of hidden Chua attractors led to the emergence of the *theory of hidden oscillations* [6,14,15], which represents the genesis of the modern era of Andronov's theory of oscillations and has attracted attention from the world's scientific community (see, e.g., [16] and references within).[1]

---

[1] In 2021 the Afraimovich Award was granted to N. Kuznetsov for *the theory of hidden oscillations and stability of dynamical systems* by the Nonlinear Dynamics and Complexity conference series.

In this work, using the Chua circuit as an example, we demonstrate the features of circuit simulation and the possibility of observing hidden attractors in a radiophysical experiment, and also compare the results obtained with mathematical modeling. For this, a special electronic circuit has been developed, which complements the Chua circuit, allowing to adjust the initial conditions. To analyze the dynamics of the Chua circuit, we consider the following models: a model at the radiophysical level (radiophysical implementation and block diagram of the Chua circuit), a model at the level of radiophysical mathematical relations (radiophysical mathematical model of the Chua circuit) and the classical (idealized) mathematical model of the Chua circuit in the phase space of dimensionless variables.

The work is structured as follows. In Sect. 2, we present the Chua circuit diagram, its derivation, and the relations between the schematic and mathematical models. We pay special attention to the definition and role of the initial conditions in the schematic model. In Sect. 3, we present the results of numerical modeling of a mathematical model for two different configurations of the structure of the phase space with hidden attractors and also consider the current–voltage characteristic (further on, $I–V$ curve) of the model to determine the possibility of realizing such parameters in a physical experiment. Then we carry out a bifurcation analysis of the mathematical model depending on the parameters characterizing the $I–V$ curve, determine the regions and characteristic $I–V$ curve for the existence of hidden attractors and also describe the bifurcation scenarios of the birth of hidden attractors and their transformation into self-excited ones. In Sect. 4, we present the results of an experiment in which the initial conditions are changed, which allow us to visualize hidden attractors in practice. In Sect. 5, using the harmonic balance method, the initial conditions for the visualization of hidden attractors are analytically determined and the results of numerical and physical experiments are compared.

2 Schematic diagram and mathematical model of the Chua circuit

The Chua circuit (see Fig. 1a) was proposed in 1983 by Leon Chua [1,17] as the simplest electrical circuit that demonstrates the regimes of chaotic oscillations.
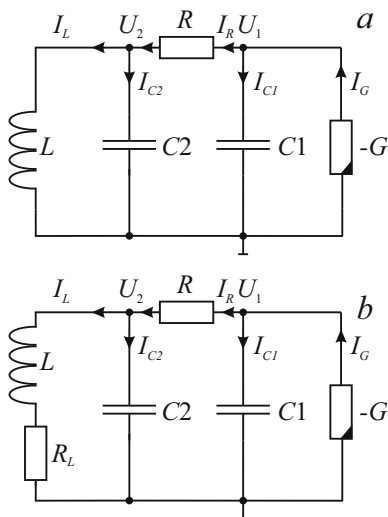
Fig. 1 Simplified scheme of the Chua circuit

The circuit consists of an inductor L, capacitors $C1$ and $C2$, a linear resistor R, and a nonlinear element with negative conductivity $-G$, commonly called the Chua diode.

To describe and analyze the dynamics in physical processes various mathematical models and their properties can be used. The dynamics obeys physical laws, which in our case can be described by a mathematical model in the form of ODEs $\dot{u} = \frac{du}{dt} = g(u, p)$, where u is the vector of system states, p is the vector of parameters, and t is the time (from zero to infinity). This model may have equilibria $u_e(p) : g(u_e(p), p) = 0$, or one can always supplement the model by additional variable $v = t$ and equation $\dot{v} = 1$, so the new model has no equilibria. Following this way for the Chua circuit in Fig. 1 we derive corresponding mathematical model from Kirchhoff's laws:

$$\begin{aligned} I_G &= I_{C1} + I_R, \\ I_R &= I_{C2} + I_L, \\ U_L &= U_2, \end{aligned} \tag{1}$$

where $I_{C1} = C1\,\dot{U}_1$, $I_{C2} = C2\,\dot{U}_2$, $I_R = (U_1 - U_2)/R$, $I_G = -G(U_1)\,U_1$. In a real physical experiment, one should take into account the parasitic resistance of the inductor L, which physically corresponds to the resistor R_L connected in series to the inductor (Fig. 1b). The voltage of such a resistor is $U_{R_L} = R_L I_L$, which is added to U_L. The current flowing through the inductor is described by the following relationship: $U_L = L\dot{I}_L$. Taking into account all the presented

relations, we obtain the following system of equations describing the circuit in Fig. 1b:

$$\begin{aligned} C1\dot{U}_1 &= -(U_1 - U_2)/R + I_G(U_1), \\ C2\dot{U}_2 &= (U_1 - U_2)/R - I_L, \\ L\dot{I}_L &= U_2 - R_L I_L. \end{aligned} \tag{2}$$

For $R_L = 0$, system (2) describes the circuit without taking into account the parasitic resistance of the inductor L (see Fig. 1a).

The Chua diode is an element with a piecewise linear I–V curve $I_G(U_1)$ having 3 segments with a negative slope. Such an element can be implemented in various ways. The classical one is the configuration of two operational amplifiers (op-amps), which was used in the first implementation [18] of the original circuit designed by Chua in [19, see Fig. P4.12]. Other realizations with op-amps as well as semiconductor diodes and transistors [20,21] are possible. In [22], the implementation of the Chua diode as an integrated device with adjustable I–V curve is presented. In [23,24], one can find detailed descriptions for physical realizations of the Chua circuit via standard off-the-shelf electronic components.

In this work, we compare the results of mathematical modeling and experiment and show the effects associated with the emergence of hidden attractors. For that, we consider the simplest implementation, which makes it easy to control the I–V curve. The Chua diode with an adjustable I–V curve is most easily implemented using op-amps. Figure 2a shows a diagram of the Chua circuit, in which the diode (highlighted by a rectangle in the diagram) is realized using circuits based on op-amps DA1.1 and DA1.2. The Chua diode contains two negative conducting elements. The first element is assembled with the op-amp DA1.1 and has a negative small-signal conductance equal to $G_1 = -(\frac{R4+R3}{R4} - 1)/R1$, where the ratio $K_1 = \frac{R4+R3}{R4} > 1$ defines the gain of DA1.1. Similarly, the second element is assembled with the op-amp DA1.2 and has a negative small-signal conductance equal to $G_2 = -(\frac{R6+R5}{R6} - 1)/R2$, where the ratio $K_2 = \frac{R6+R5}{R6} > 1$ defines the gain of DA1.2. Without loss of generality, we assume that K_1 is larger than K_2. Thus, each of these sub-circuits represents a piecewise linear element with a negative small-signal resistance, and, in parallel, these two elements form the I–V curve of the entire Chua diode.

The principle of operation for a negative small-signal resistance at a DC operating point implemented with an op-amp can be described as follows: the input

Fig. 2 **a** The Chua circuit implemented with op-amps, **b** experimental $I-V$ curve of the Chua diode
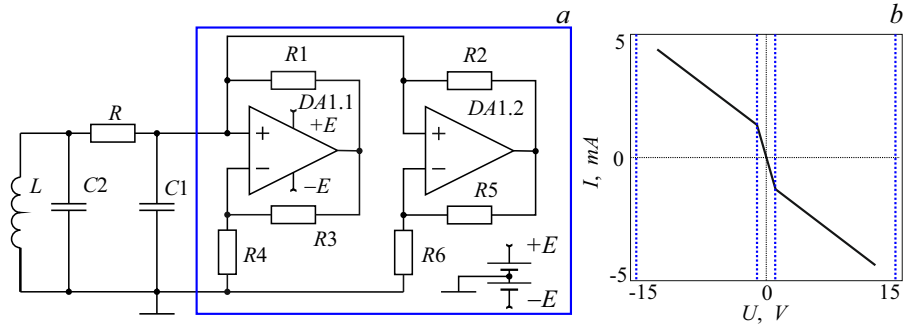
voltage is linearly amplified with the gain of the op-amp; however, the small-signal resistance of the entire circuit is negative. When the op-amp's output voltage becomes equal to the saturation voltage, the op-amp switches to saturation mode and the circuit's small-signal resistance becomes positive. Thus, a configuration of two op-amps in parallel makes it possible to implement a piecewise linear $I-V$ curve by setting proper values of gains. In the range of input voltages $[-U_{DA1}, U_{DA1}]$ both op-amps DA1.1 and DA1.2 operate in amplification mode with total negative conductance $G_1 + G_2$. When the input voltage is increased and reaches intervals $[-U_{DA2}, -U_{DA1}) \bigcup (U_{DA1}, U_{DA2}]$, the op-amp DA1.1 switches to the saturation mode and thus the total negative conductance is determined by the negative conductance introduced by the DA1.2 op-amp circuit and the positive conductance introduced by the DA1.1 op-amp circuit. The total conductivity is equal to $1/R1 + G_2$, while the slope angles of the $I-V$ curve are changed. With a further increase in the input voltage beyond the interval $[-U_{DA2}, U_{DA2}]$, both op-amps operate in the saturation mode and their total conductance becomes positive, equal to $1/R1 + 1/R2$. Figure 2b shows the $I-V$ curve of the Chua diode, obtained in a physical experiment; it has three linear sections. The parameters of experimental model are selected in such a way that the bounded phase trajectories (in the limit) do not reach the second break points $-U_{DA2}$, U_{DA2}, since the mathematical model of the Chua circuit takes into account only the first break points $-U_{DA1}$, U_{DA1}. The tilt angles of different sections of the $I-V$ curve can be varied by changing the values of $R1-R6$. The breakpoints of the $I-V$ curve determine the voltages U_{DA1} and U_{DA2} as follows:

$$\pm U_{DA1} = \pm E \frac{R4}{R3+R4} = \pm E/K_1,$$
$$\pm U_{DA2} = \pm E \frac{R6}{R5+R6} = \pm E/K_2, \tag{3}$$

where E is the DC supply voltage of the circuit. Thus, in general terms, the small-signal conductance $G(U_1)$ at the DC operating point U_1 of the $I-V$ curve of the Chua diode shown in Fig. 2a is described by the following

$$G(U_1) = \begin{cases} G_1 + G_2, & |U_1| \leq U_{DA1} \\ \frac{1}{R1} + G_2, & \begin{array}{l} U_{DA1} < U_1 \leq U_{DA2}, \\ -U_{DA2} \leq U_1 < -U_{DA1} \end{array} \\ \frac{1}{R1} + \frac{1}{R2}, & |U_1| > U_{DA2}. \end{cases} \tag{4}$$

Introducing new dimensionless normalized dynamical variables: $x = U_1/U_{DA1}$, $y = U_2/U_{DA1}$, $z = -I_L R/U_{DA1}$, the piecewise linear function describing the $I-V$ curve of the Chua diode can be written as follows:

$$f(x) = \begin{cases} R[G_1 + G_2]x, & |x| \leq 1 \\ R[\frac{1}{R1} + G_2]x - \frac{RK_1}{R_1}, & 1 < x \leq \frac{U_{DA2}}{U_{DA1}}, \\ R[\frac{1}{R1} + G_2]x + \frac{RK_1}{R_1}, & -\frac{U_{DA2}}{U_{DA1}} \leq x < -1, \\ R[\frac{1}{R1} + \frac{1}{R2}]x - [\frac{RK_1}{R_1} + \frac{RK_1}{R_2}], & x > \frac{U_{DA2}}{U_{DA1}}, \\ R[\frac{1}{R1} + \frac{1}{R2}]x + [\frac{RK_1}{R_1} + \frac{RK_1}{R_2}], & x < -\frac{U_{DA2}}{U_{DA1}}. \end{cases} \tag{5}$$

Figure 3 shows the $I-V$ curve corresponding to function (5), which depicts all five different linear segments. For a rigorous in-depth analysis of the two op-amp circuits (connected in parallel) inside the rectangle in Fig. 2a, the reader is referred to Chapter 4 of [19], and [25].

After performing the following renormalization of time: $\tau \rightarrow \frac{1}{C2R}t$, and taking into account (19), we obtain the following system of equations in dimensionless form:

$$\dot{x} = -\alpha(x - y) - \alpha f(x),$$
$$\dot{y} = z - (y - x), \tag{6}$$
$$\dot{z} = -\beta y - \gamma z,$$

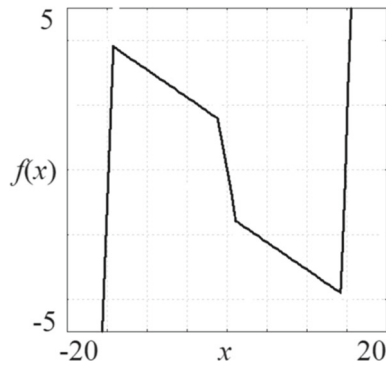where $\alpha = C2/C1$, $\beta = C2R^2/L$, $\gamma = C2RR_L/L$.

Fig. 3 Complete theoretical I–V curve of the Chua diode, taking into account all 4 break points (3). The I–V curve is odd-symmetric. The innermost breakpoints are located at $|x| = 1$; the outermost breakpoints are located at $|x| = \frac{U_{\text{DA2}}}{U_{\text{DA1}}}$
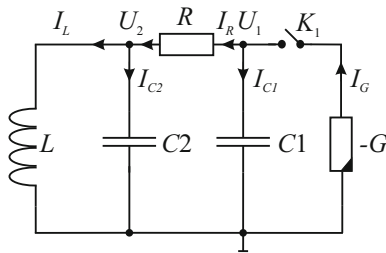

Fig. 4 The Chua circuit diagram with the on/off switch K_1

Multistability is a fairly common phenomenon that arises not only in radiophysical systems, but also in various abstract problems of mathematics (see, e.g., the *16th Hilbert problem* [26]) and engineering problems (see, e.g., [6,14,27–34]). Prediction and investigation of coexisting regimes, especially if they are hidden, is a rather difficult task that is important for various engineering applications (see, e.g., phase-locked loops [35–39]). One of the most important questions in the study of multistable systems, especially with hidden attractors, is the choice of the initial conditions to reveal all possible limiting regimes. This problem is much easier to solve in numerical simulation; setting the initial conditions is an obligatory part for the initial value problem (IVP). However, even numerically, the search for attractors with small basins of attraction in the phase space (rare attractors) and hidden attractors may be an essentially nontrivial problem and require additional research methods [6].

In a physical experiment, it is rather difficult to control the choice of the initial conditions. If we talk about a radiophysical experiment with the Chua circuit then the

initial conditions are the starting voltages on the capacitors $C1$ and $C2$, as well as the current in the inductor I_L at the moment of starting the setup. Traditionally, without additional sub-circuits, the initial conditions are determined by the voltages across the capacitors and the current in the inductor at the moment the circuit is switched on and at this moment are zero. This corresponds to the situation when the circuit switched off at the moment when the power supply is turned off. Figure 4 shows a diagram of the Chua circuit, in which the switch K_1 can be used to open and close the circuit. When the switch K_1 is open, the capacitors are discharged; the current in the inductor is zero. Thus, when the circuit is closed, the system starts from zero initial conditions. In a real physical experiments, the closed circuit is usually triggered by supplying power E to the op-amps (see Fig. 2). Usually in the literature, only closed circuit is considered (see Fig. 1, [2,17]), which leads to the fact that the question of initial conditions for starting the circuit is ignored.

For the mathematical modeling we use the Chua circuit model in form (6), and the I–V curve of the Chua diode is considered as a piecewise linear function of the following form:

$$f(x) = m_1 x + \tfrac{1}{2}(m_0 - m_1)(|x + 1| - |x - 1|), \quad (7)$$

with the following expressions for the slope coefficients [according to (5)]:

$$m_0 = R\left(-\frac{R3}{R4R1} - \frac{R5}{R6R2}\right), \ m_1 = R\left(\frac{1}{R1} - \frac{R5}{R6R2}\right). \tag{8}$$

In this form, the system of differential equations for the Chua circuit was first proposed and is most often used in literature. Note that piecewise linear function (7) does not fully match I–V curve (5). Function (7) does not have the second pair of symmetric break points, since the third linear segment corresponds to the saturation mode of op-amps, which in a physical experiment does not allow the values of quantities corresponding to the variables of system (6) to escape to infinity. However, the main dynamics of system (6) evolves on the basis of the first break points of the I–V curve; the phase trajectories do not enter the region of the phase space $|x| > \frac{U_{\text{DA2}}}{U_{\text{DA1}}}$, which leads to the fact that the mathematical model and the experimental circuit are in good agreement.

Within the framework of this paper, we reproduce in a real physical experiment the results of numerical simulation and demonstrate various bifurcations of the birth of hidden attractors in the Chua circuit.

3 Mathematical modeling of dynamical regimes and bifurcations in the Chua circuit

For the bifurcation analysis, the equilibria play an important role. If the mathematical model has a known periodic orbit (limit cycle) $u(t, u_0) = u(t + T, u_0)$, i.e., the initial data u_0 and the period T are known in advance, then it is possible to construct a mathematical model represented the discrete dynamics of the original system on the Poincaré section, which has an equilibrium state corresponding to the periodic orbit. In this regard, following [40, p. 81], [41, p. 10–11], [42, p. 58–59], for the chosen mathematical model, a *local bifurcation* is a qualitative restructuring of the model's behavior in an arbitrarily small neighborhood of the equilibrium state during a process that continuously depending on a parameter when the parameter passes through the critical (bifurcation) value; the bifurcations that cannot be detected by considering an arbitrarily small neighborhood of equilibria are called *global bifurcations*. Also in this classification, one can separate out a class of bifurcations in small vicinity of unstable manifolds of equilibrium states (e.g., the birth of homoclinic or heteroclinic orbits and self-excited chaotic attractors). For the analysis of local bifurcations, various analytical methods are well developed (see, e.g., [40,42–44]), while the analysis of global bifurcations is often a challenging task. For example, the identification of global bifurcations associated with the birth or destruction of hidden attractors is the key task in the analysis of the boundaries of global stability regions (the case of attraction of all system's trajectories to the stationary set consisting of the equilibrium points) in the parameter space. The parts of the global stability boundary in the space of parameters associated with global bifurcations and the birth of hidden oscillations are called *hidden* parts of the global stability boundary [6,14–16,45], while the loss of global stability through local bifurcations in vicinity of the stationary set corresponds to *trivial* parts. The difficulties of studying global bifurcations and hidden attractors can be demonstrated by Hilbert's 16th problem [40,41,46]).

Chua system (6)–(7) has five control parameters α, β, γ, m_0, and m_1. It is shown in [5] that for fixed $\alpha = 8.4$, $\beta = 12$, $\gamma = -0.005$ on the parameter plane (m_0, m_1), there are two regions corresponding to the existence of two configuration of hidden attractors.[2] The parameters α, β and γ in the Chua system are determined by the elements of the oscillatory sub-circuit, while the parameters m_0 and m_1 are set by the I–V curve of the active nonlinear element. Thus, depending on the I–V curve of the Chua diode, hidden attractors can be realized in the system.

Model (6) may have one or three equilibria depending on the relations between the parameters. There is always the equilibrium state ($u^0 = (x^0, y^0, z^0) = (0, 0, 0)$), and for some values of the parameters,[3] two additional symmetric equilibria with coordinates:

$$u_S^{1,2} = (\pm u_x, \pm u_y, \mp u_z), \tag{9}$$

where

$$u_x = u_y + u_z, \quad u_y = \frac{\gamma(m_0 - m_1)}{\gamma m_1 + \beta m_1 + \beta},$$
$$u_z = \frac{\beta(m_0 - m_1)}{\gamma m_1 + \beta m_1 + \beta},$$

can arise.

Consider examples of hidden attractors with different configurations. Figure 5 shows examples of hidden attractors for two points of the parameter plane corresponding to two different regions with hidden attractors.[4] Figure 5a–c shows illustrations for the first region, for parameters $\alpha = 8.4$, $\beta = 12$, $\gamma = 0$, $m_0 = -0.12$, and $m_1 = -1.15$. In this case, two symmetric coexisting chaotic attractors are observed in the system. At the origin there is a stable focus with eigenvalues $\lambda_1 = -8.348114$, $\lambda_{2,3} = -0.021943 \pm i3.259625$, and there are also two symmetric unstable equilibria with coordinates ($\pm 6.8667, 0, \mp 6.8667$) and eigenvalues $\lambda_1 = 2.236517$, $\lambda_{2,3} = -0.988258 \pm i2.404965$. Trajectories from the vicinity of these two saddle-foci tend either to the stable zero equilibrium or to infinity. Figure 5a shows the structure of the phase space; different colors indicate trajectories starting from different initial conditions: gray and black lines indicate the trajectories tending to hidden attractors; red and pink colors indicate the trajectories starting from a neighborhood of symmetric equilibria. In Fig. 5b and c, the two-dimensional planes of initial conditions for vicinities of equilibrium points are shown

---

[2] Slightly varying of parameters α, β, γ does not change main structure of the bifurcation lines on the parameter plane (m_0, m_1) and one can also find both configuration of hidden attractors.

[3] In [9], the regions of existence of three equilibria are described in more details.

[4] We solve numerically ODE with 4th-order Runge–Kutta method with integration step 10^{-3}.
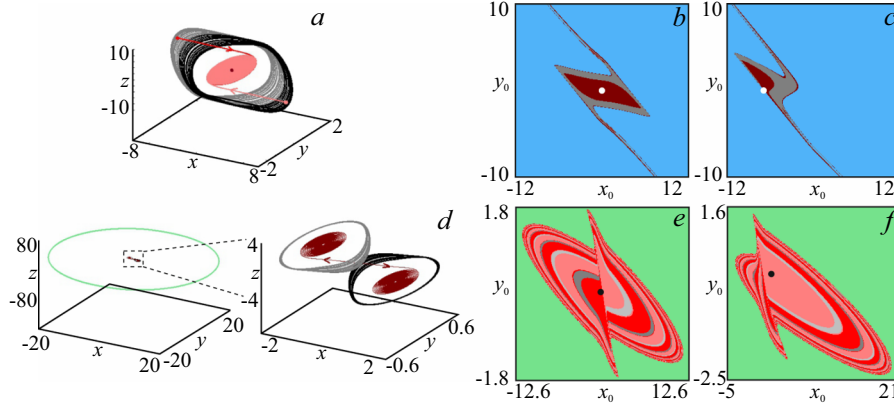
Fig. 5 Phase portraits and attractors of the Chua system with parameters $\alpha = 8.4$, $\beta = 12$, $\gamma = 0$, $m_0 = -0.12$, and $m_1 = -1.15$ (see **a**); with parameters $\alpha = 8.41$, $\beta = 12.23$, $\gamma = 0.0435$, $m_0 = -1.366$, and $m_1 = -0.17$ (see **d**). For the attractors, 2D cross sections of their basins of attraction for $\alpha = 8.4$, $\beta = 12$, $\gamma = 0$, $m_0 = -0.12$, $m_1 = -1.15$ with $z_0 = 0.001$ (see **b**), and with $z_0 = 6.868$ (see **c**); for $\alpha = 8.41$, $\beta = 12.23$, $\gamma = 0.0435$, $m_0 = -1.366$, $m_1 = -0.17$ with $z_0 = 0.001$ (see **e**), and $z_0 = 1.443$ (see **f**)

(here we consider the Poincaré cross section by plane $z = 0$). The regime of divergency[5] is marked by blue color, the basin of attraction[6] of the stable zero equilibrium is marked by maroon color. The basins of attraction of chaotic[7] attractors are denoted by gray color. The projections of the equilibrium points in the plane are identified by white dots. Figure 5b shows a two-dimensional plane of initial conditions for fixed $z_0 = 0.001$ in the vicinity of the zero equilibrium u^0 (stable focus). Figure 5b shows the structure of the basins of attraction for two coexisting regimes. There is a rather large basin of attraction surrounding the stable zero equilibrium (maroon color), and a large area of divergency. The zero stable equilibrium point is located in the center of the basin of attraction; consequently,

choosing initial conditions from a neighborhood of zero equilibrium, the corresponding trajectory may not leave beyond its basin of attraction. Between these two areas we have an area of chaotic oscillations, which represents the basins of attraction of chaotic attractors. Between the areas of divergency and attraction area of chaotic attractor one can find a thick area, which corresponds to the stable zero equilibrium basin attraction. In Fig. 5c is shown a vicinity of one of the symmetric points $z_0 = u_z = -6.8665$ (saddle-focus). The basin of attraction for the stable zero equilibrium u^0 at the center is combined with the another part of the basin of attraction for the stable zero equilibrium point u^0 on the boundary of the area of divergency, and a projection of saddle equilibrium u_S^1 is located on the boundary between the basin of attraction for the stable zero equilibrium point and the area of divergency. Consequently, a chaotic attractors are hidden because if we choose initial states near one of the equilibrium points, then we cannot reach the chaotic attractors.

Figure 5d–f shows the results of a similar study of hidden attractors for the second region of the parameter space with $\alpha = 8.41$, $\beta = 12.23$ $\gamma = 0.0435$, $m_0 = -1.366$, and $m_1 = -0.17$. For the second region, the zero equilibrium is a saddle-focus with two-dimensional stable and one-dimensional unstable manifolds (corresponding eigenvalues are $\lambda_1 = 4.12175$ and $\lambda_{2,3} = -1.043595 \pm i2.857504$), and symmetric equilibria (∓ 1.4471, ∓ 0.005129, ± 1.442), which

---

[5] Regime of divergency corresponds to the regime, when the dynamical variables numerically grow to infinity, the detection of this regime is realized under the condition $\sqrt{x^2 + y^2 + z^2} > 1000$.

[6] In the numerical experiment, we do not analyze nontrivial invariant sets of measure zero (for example, saddle periodic trajectories and their stable and unstable manifolds), and the visualization of attraction basins on a bounded area of the Poincaré section may not reflect them properly.

[7] In the experiments with direct numerical integration, chaos is often manifested if there is a positive finite-time local Lyapunov exponent along a trajectory (see, e.g., [47–49]), or if there is a sufficiently large number of different points in a bounded domain (e.g., more than 120 in our experiments) in the corresponding numerical experiments with the Poincaré section.

are stable foci with eigenvalues $\lambda_1 = -7.968363$ and $\lambda_{2,3} = -0.027719 \pm i3.271839$. In Fig. 5d from the vicinity of the unstable equilibrium state (maroon color), the phase trajectories arrive at one of the symmetric stable foci. Also, a pair of symmetric chaotic attractors coexists in the phase space. With this choice of parameters, a stable hidden limit cycle of a large amplitude is also observed in the phase space, within which all other discussed coexisting limiting regimes are located.

Figure 5e and f shows the structure of basins of attraction for different cross sections of the phase space, including the basins of attraction of coexisting attractors in the vicinity of the stable focus u_S^1 and in the vicinity of the zero saddle equilibrium, respectively. The projections of equilibrium points are marked in the plane by black dots. We shaded the basins of attraction of different symmetric chaotic attractors by the gray colors (light and dark). The basin of attraction of the external limit cycle is marked in the plane by the light green color. We use the pink and red colors to denote the basins of attraction of the two symmetric equilibria u_S^1 and u_S^2, respectively. Firstly, we consider a plane of initial conditions and the basins of attraction of different attractors in the vicinity of the saddle equilibrium point (Fig. 5e). We can see that the phase trajectories starting from the vicinity of the saddle point can reach only one of the stable symmetric equilibria. The zero equilibrium point u^0 is located on a boundary between the attracting areas of symmetric stable equilibria. The basins of attraction are symmetric to each other, and the boundary between these areas (a curve between the basins of attraction of different stable equilibria near zero) represents the cross section of stable two-dimensional manifold of the zero saddle-focus. Consequently, if we choose initial conditions in the vicinity of any equilibrium point, we reach one of the stable equilibrium points and, thus, all of oscillatory attractors are hidden attractors. Then, we consider a vicinity of the stable equilibrium (Fig. 5f). There one can see a large basin of attraction surrounds one of the symmetric stable equilibrium points. Also, there are the basin of attraction of another symmetric stable equilibrium point, and the symmetric basins of attraction of two symmetric chaotic attractors. For these chaotic attractors, the complex structure of their basins of attraction is represented by the area of attractions in the form of bands, which are spiraled together, and their boundaries have self-similar patterns, i.e., fractal structures.

Also, there is a basin of attraction of the external stable limit cycle, which surrounds all other discussed basins of attraction.

As mentioned above, in our physical experiment we change the initial conditions of only two dynamic variables x and y corresponding to the voltages U_1 and U_2 on the capacitors of the oscillatory circuit, respectively. We do not change the initial state of the third variable z corresponding to the current in the inductor I_L. Inductor current fluctuates in small vicinity of zero. Thus, it is not possible to distinguish and reveal hidden attractors for the first region of parameters, since we do not able to set the value of the variable z to a nonzero value when closing the circuit and to investigate the neighborhood of a nonzero equilibrium state. Also, for this configuration of hidden attractors, the implementation of the regime with trajectories escaping to infinity has its own specifics. The property of a trajectory tending to infinity indicates that this trajectory falls into a region in the phase space where there is no global contraction of the phase volume, and in some sense the system becomes nondissipative having an unlimited growth of the dynamical variable. In a physical experiment, it is impossible to observe the escape of a trajectory to infinity due to the peculiarities of the operation of the op-amps: if the voltage at the output of the op-amp becomes higher than the supply voltage, then the op-amp goes into the saturation mode. In this case, in the experiment, one do not observe self-oscillations, the voltages on the capacitors are constant and equal to the supply voltage of the op-amps. This difference is a consequence of the difference between nonlinear $I–V$ curve (5) and its approximation (7). The third condition in (5) defines an additional break in the $I–V$ curve (which, however, is outside the dynamics we are considering for the second configuration of attractors). For the first configuration of attractors, this feature leads to the fact that instead of the "escape-to-infinity" regime, a stable equilibrium corresponding to the supply voltage of the circuit is observed.

For the second region in the parameter space and corresponding second configuration of attractors, the situation is different: it is fundamentally important to investigate the neighborhood of the zero equilibrium, and the neighborhoods of symmetric equilibria do not play a special role. It is also worth noting that such a configuration is richer in terms of multistability: it assumes possibility to observe five attractors, three of which are hidden. This configuration of attractors pre-

viously demonstrated in [5,50–52] is quite robust to parameter changes (see works [5,51], where the corresponding structure of the parameter space is analyzed). In [5,50], the implementation of hidden attractors for the case of negative values of the parameter γ is demonstrated, while in Fig. 5d an example of the existence of hidden attractors for positive values of the parameter γ is shown.

Further in this work, we consider the parameters of the radiophysical model corresponding to the second region of the parameter space. To this end, we numerically investigate the bifurcation scenario of the birth and transition from hidden to self-excited attractors and the configuration of the $I-V$ curve only for such a choice of parameters.

In the work [5], the regions of existence of hidden attractors in a two-parameter space (m_0, m_1) are shown and scenarios of their occurrence are described. In particular, for the region of parameters interesting to us, it is shown that the external large-amplitude limit cycle appears as a result of the supercritical Andronov–Hopf bifurcation of the zero equilibrium (see, e.g., [45,53]).

Let us turn to one-parameter bifurcation analysis depending on the parameter m_1. In Fig. 6a, a bifurcation diagram built using the numerical package XPPAUT [54] is presented where with different colors we depict stable (red) and unstable (black) equilibrium points and maximum values of stable (green) and unstable (blue) limit cycles in projection into dynamical variable x (the package determines all variables). We started from stable equilibrium at $m_1 = 0$ and continuation of equilibrium point firstly was implemented with detection of the Andronov–Hopf bifurcation point. Then we started from the Andronov–Hopf bifurcation point and construct a cycle which was born near equilibrium point with standard XPPAUT command. Remark that XPPAUT allow to continue this cycle on parameter (the path in the parameter space is determined automatically) and also find and construct another cycle which was born as a result of saddle-node bifurcation. The line of cycles was constructed in one iteration. From the period-doubling bifurcation (point PD) it is possible to construct additional stable cycle, but the second round of iteration is needed for that, which was missed to avoid difficultization of the figure. In Fig. 6b and c, two bifurcation trees obtained with direct integration are shown. They were constructed with Poincaré cross section by plane $z = 0$, and Fig. 6b and c demonstrate the projection of the tree into dynamical variable x. For
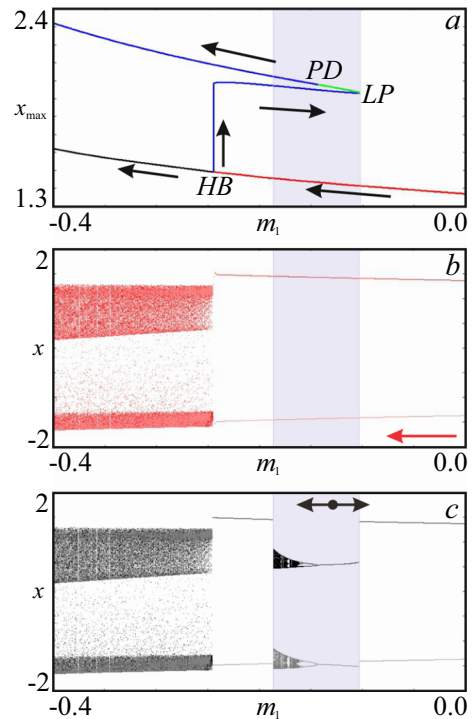

Fig. 6 Bifurcation diagram (**a**); bifurcation trees (**b**, **c**). Parameters $\alpha = 8.41$, $\beta = 12.23$, $\gamma = 0.0435$, and $m_0 = -1.366$. LP is the saddle-node bifurcation; HB is the Andronov–Hopf bifurcation; PD is the period-doubling bifurcation

parameter intervals where the equilibrium point is stable we depict x-projection position of the equilibrium point. All the diagrams are built for the parameters: $\alpha = 8.41$, $\beta = 12.23$, $\gamma = 0.0435$, and $m_0 = -1.366$.

To visualize self-excited attractors we should check the behavior of trajectories in vicinities of unstable equilibria. For Chua system (6), we should check trajectories from vicinity of saddle-focus at zero. Remark that the system is linear near zero equilibrium, there are two-dimensional stable and one-dimensional unstable manifolds, and the Jacobian matrix near zero equilibrium is independent of the parameter m_1. We verified the set of initial conditions, chosen randomly in the cube of phase space with a side 10^{-3} surrounding the zero saddle equilibrium, and we obtained the same bifurcation tree. By red and pink in Fig. 6b, we depict bifurcation trees constructed for the initial conditions fixed in the vicinity of the saddle zero equilibrium: $x_0 = 0.001$, $y_0 = 0.001$, and $z_0 = 0.001$ for the red tree; $x_0 = -0.001$, $y_0 = -0.001$, and $z_0 = -0.001$ for the pink one.

Figure 6c shows a family of bifurcation trees built with *inheritance of the initial conditions*.[8] The starting initial conditions for the tree shown in black (see Fig. 6a) are chosen on the hidden attractor at $m_1 = -0.12$ ($x_0 = 0.55$, $y_0 = -0.36$, $z_0 = 0.00$). From this point we scan a parameter interval in two directions, defined by increasing, or decreasing parameter m_1, and apply inheritance of the initial conditions. For the gray tree, the starting point is chosen on the symmetric hidden attractor.

Thus, as the parameter m_1 increases, the following bifurcation transitions can be observed. At $m_1 = -0.4$, the system has two coexisting symmetric saddle equilibria (saddle-foci with two-dimensional unstable manifold); the system also contains a saddle-focus with a one-dimensional unstable manifold. At $m_1 \approx -0.2447$, saddle-foci with two-dimensional unstable manifold undergo the Andronov–Hopf bifurcation (*HB*) and become stable. This bifurcation is subcritical, and a saddle limit cycle is born. The cycle has a relatively large amplitude because system (6) is piecewise linear and the equilibrium is a center at the Andronov–Hopf bifurcation point. With further increasing of the parameter m_1 at $m_1 \approx -0.1031$, as a result of a saddle-node bifurcation (see point *LP* in Fig. 6a), the saddle cycle is merged with another stable limit cycle (one pair of cycles is shown in Fig. 6a; the other pair is obtained due to the presence of symmetry in the system), which coexists with stable equilibria. Such a configuration is typical for the subcritical Andronov–Hopf bifurcation and can be associated with the co-dimension-2 Bautin bifurcation [42]. The limit cycles are located in such a way that from the vicinity of the equilibria, including the saddle-focus with one-dimensional unstable manifold, a phase trajectory is attracted to one of these equilibria; thus, these stable limit cycles are hidden. As the parameter m_1 decreases, the stable limit cycles undergo a period doubling bifurcation (at $m_1 \approx -0.1441$ labeled with *PD* in Fig. 6a). The bifurcation trees (Fig. 6c) show a cascade of period doubling bifurcations forming coexisting hidden chaotic attractors. At $m_1 \approx -0.186$, chaotic attractors are collapses as a result of the crisis [55,56] and the trajectories tend to equilibria. For $m_1 < -0.2447$, equilibrium points become unstable

and trajectories from the vicinity of the zero unstable equilibrium begin to reach the chaotic attractor. At the same time, it is clearly seen on the bifurcation tree (Fig. 6b, c) that symmetric chaotic attractors have already merged into one chaotic attractor; however, this attractor is already self-excited. Such bifurcations[9] form a structure of bifurcation tree with gap between hidden and self-excited attractors, where stable equilibrium states are dominant. To guarantee the absence of other hidden attractors one may carry out a detailed analysis of the structure for basins of attraction in the same way as in Fig. 5b, c, e, and f.

Thus, with the considered change in the parameters and for the given range, hidden attractors arise as a result of a saddle-node bifurcation of the production of two pairs of cycles, and undergo a crisis, which leads to their collapse. Subsequently, they transform into a merged self-excited attractor through the subcritical Andronov–Hopf bifurcation. In Fig. 6c, the interval of the parameter m_1, corresponding to the existence of hidden attractors, is marked in purple. Remark that in our experiments the attractors are revealed by the standard integration (fourth-order Runge–Kutta method), and the obtained results are in a good agreement with physical experiments. At the same time, more accurate numerical methods (see, e.g., [58,59]) may help to reveal other attractors and repellers in the mathematical model, which we do not observe in the physical model due to the presence of noise.

Let us move on to consider the features of the nonlinear function that characterizes the *Chua diode*. As mentioned earlier, the nonlinear $I–V$ curve is a piecewise linear function, different sections of which have different tilt angles, which in the experiment are controlled by resistors connected to op-amps within the Chua diode. For mathematical modeling, the $I–V$ curve of this element is approximated by piecewise linear function (7), in which the tilt angles of various linear sections are controlled by the parameters m_0 and m_1 [17]. When changing only the parameter m_1, the central part of the $I–V$ curve in the range $(-1, 1)$ remains unchanged, and the angle of the side branches changes. Varying the parameter m_0 leads to a change in the angle of the central part of the curve within the range $(-1, 1)$. Figure 7

---

[8] For each new value of the parameter, the initial conditions are chosen as the final state attained for the previous value of the parameter.

[9] In [57] such global bifurcation is called a hidden bifurcation, since it is not seen during the numerical bifurcation analysis from a small neighborhood of the equilibrium states by direct integration.
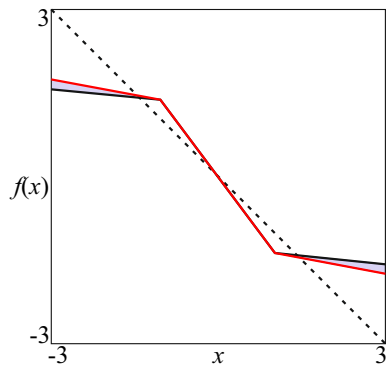
Fig. 7 Graphs of the function $f(x)$ (7), which is an approximation of the $I–V$ curve of the Chua diode. The $I–V$ curve configurations in which hidden attractors can be observed are marked in purple

shows the graphs of the nonlinear function $f(x)$ for the critical values of the parameter m_1 which correspond to the existence of hidden attractors: the black line for $m_1 = -0.1031$ corresponds to the saddle-node bifurcation point, which resulted in appearing of a hidden attractor; the red line for $m_1 = -0.186$ corresponds to the crisis point of the hidden chaotic attractor. Thus, in this graph, we can distinguish the regions corresponding to different dynamics of the system and different types of attractors. The purple areas correspond to the existence of three hidden attractors.

In general case, numerical analysis of dynamics via direct integration or by using Poincaré sections suffers from the accuracy of determining stationary points, the corresponding periodic trajectories, their periods, and initial data (which can fill an unbounded domain of the phase space, e.g., as in example (36)), numerical integration of irregular and unstable trajectories (e.g., for the Lorenz system, the shadowing theory gives a rather short time interval of reliable integration for the standard numerical procedure and parameters of tolerances [49,60]), as well as identifying chaotic behavior by finite-time local Lyapunov exponents (which can change their signs as the time interval of integration is increasing [49]). Also, there are classes of systems for which the application of the analysis of dynamics on a Poincaré section to reveal and analyze hidden attractors may not be straightforward. These are, for example, multidimensional ODEs and difference systems (where the choice of Poincaré sections may not be obvious); systems with fractional derivative operators (which do not have periodic solutions at all [61]); systems with a

cylindrical phase space that can have a global attractor without equilibria [62] and systems without equilibria and with local attractors in Euclidean space; as well as discontinuous systems (where the birth of attractors may be essentially determined by the behavior of the system on the discontinuity surface, see, e.g., [63–66]) and systems with uncountable and unbounded set of equilibrium states (see, e.g., [67]).

4 Experimental observation of dynamical regimes in the Chua circuit

Now let us turn to the experimental study and visualization of the hidden attractors. As it is mentioned above, we are able to implement the changing of two initial conditions x_0 and y_0 related to capacitor voltages $C1$ and $C2$ at the moment the circuit is turn on. The circuit implementation for changing the third initial condition corresponding to the inductor current is more difficult and is not included in this work. As one can see from the structure of the basins of attraction, for checking the regime discussed above, it is enough to vary one initial condition. Hence, we keep the voltage on the second capacitor $C2$ satisfying the zero initial condition.

Figure 8a shows the schematic diagram of the Chua circuit with an additional block that allows us to control the initial conditions. Figure 8b presents a photograph of the experimental setup. To control the operation of the circuit and set the initial conditions, electronic keys (multiplexors) DD1 and DD2 are added to the circuit. With a zero signal at the input (In), the key 01 of the multiplexor DD1 connects the capacitor $C1$ to point **1**, and the key 11 connects the capacitor $C2$ to point **2**. Keys 01, 11 of the multiplexor DD2 are connected to the inputs of the op-amps DA1.1, DA1.2, respectively, as shown for the Chua circuit in Fig. 2. When a high logic level is applied to the input (In), the keys 01 and 11 of the multiplexor DD1 open, and keys 00 and 10 close, connecting the capacitors $C1$ and $C2$ to the sliding contacts of potentiometers $R7$ and $R8$, respectively. At the same time, keys 01 and 11 of the multiplexor DD2 also open, turning off the negative resistance block for the duration of the pulse. In Table 1, we summarize states of electronic keys DD1, DD2 depending on the control input parameter (In).

We can change the voltage at the sliding contacts of potentiometers $R7$ and $R8$ during the experiment by adjusting manually the initial voltages of the capaci-
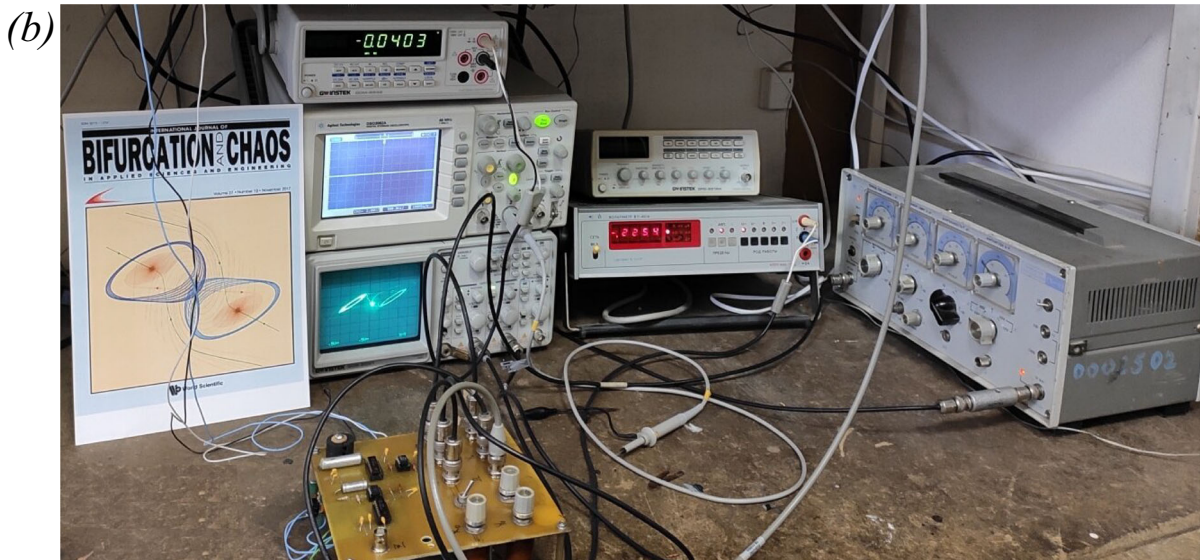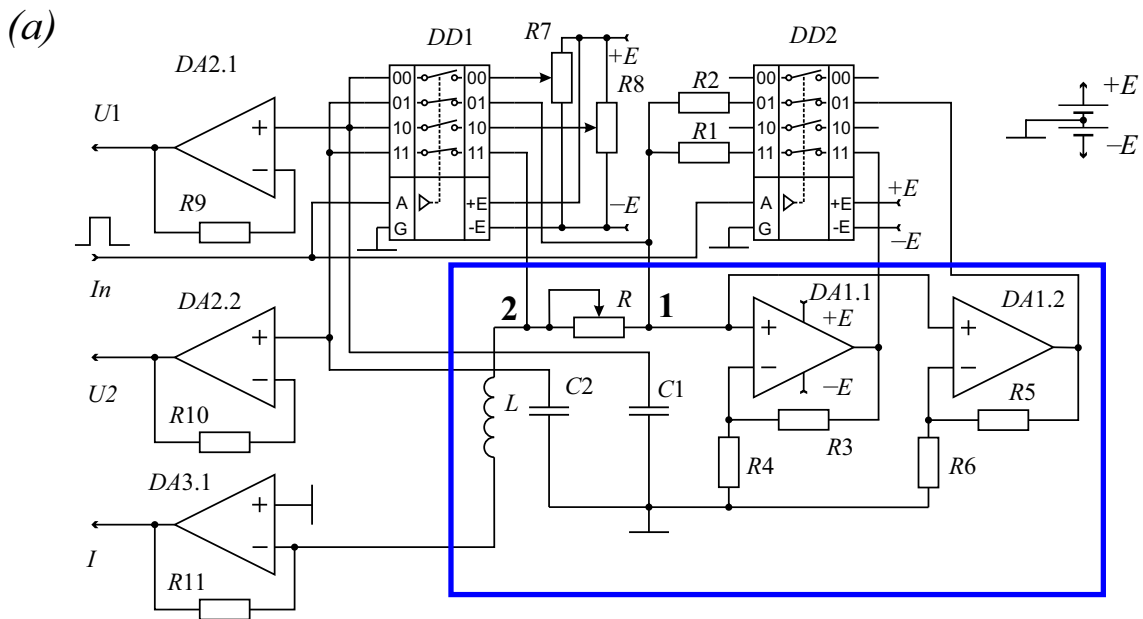
Fig. 8 a Schematic diagram of the experimental Chua circuit with switches for changing initial conditions; **b** the photograph of the experimental laboratory model and the IJBC journal cover

with hidden Chua attractors [5]. The classical Chua circuit is marked with a blue rectangle

tors. Thus, when rectangular pulses of duration T_{imp} with a repetition period T are applied to the input (In), throughout the pulse, the capacitors charge to some initial values, and at the end of the pulse, the circuit is switched to the normal operation of the generator with

the fixed/specified initial conditions. During the experiment, we apply a pulse signal to the input (In) and changed the voltage at the sliding contacts of potentiometers $R7$ and $R8$, thereby controlling the initial conditions. Using a two-channel oscilloscope operat-

Table 1 States of electronic keys DD1, DD2 depending on the control input parameter In

In	DD1 00	DD1 01	DD1 10	DD1 11	DD2 01	DD2 11
0	Open	Close	Open	Close	Close	Close
1	Close	Open	Close	Open	Open	Open

ing in the X–Y mode, we observe transient processes in the circuit, stable and unstable limit cycles and equilibrium points. The period T and the duration of the pulses T_{imp} are selected so that the charging time of the capacitors is less than $(T - T_{\text{imp}})$. A similar technique is used to study transient processes and basins of attraction of multistable systems in [68]. Op-amps DA2.1, DA2.2 and DA3.1 are voltage buffers, or so-called decoupling amplifiers, which are needed to ensure measuring circuits, do not affect the operation of the main circuit. Here, for the experimental setup we use op-amps AD822 (see, e.g., [69]).

To detect hidden oscillations, the nominal values for the experimental scheme are carefully calculated so that they corresponded to the values of the model parameters. The nominal values of the oscillatory circuit are fixed as follows:

$$C1 = 311\,\text{nF}, C2 = 37\,\text{nF}, L = 15.79\,\text{mH}, \\ R = 788\,\Omega, R_L = 2.8\,\Omega. \tag{10}$$

For these nominal values, the dimensionless parameters of the model α, β, and γ are as follows: $\alpha = \frac{C2}{C1} \approx 8.4054$, $\beta = \frac{C2R^2}{L} \approx 12.2301$, and $\gamma = \frac{C2RR_L}{L} \approx 0.0435$. The slopes of the linear pieces and the break points of the I–V curve are determined by potentiometers $R1$–$R6$: $R1 = 8520\,\Omega$, $R2 = 123\,\Omega$, $R3 = 12.02\,\text{k}\Omega$, $R4 = 1008\,\Omega$, $R5 = 1003\,\Omega$, $R6 = 24.41\,\text{k}\Omega$. Thus, in the experiment, the amplification coefficients are: $K_1 = 12.9246$, $K_2 = 1.0411$, consequently, and $U_{\text{DA1}} = 1.1606\,\text{V}$, $U_{\text{DA2}} = 14.408\,\text{V}$. The slope of the central piece of the I–V curve inside the interval from $-U_{\text{DA1}}$ to U_{DA1} equals $G_1 + G_2 = -0.001\,734\,\text{S}$. For the next intervals, from $-U_{\text{DA2}}$ to $-U_{\text{DA1}}$ and from U_{DA1} to U_{DA2}, the slope is $1/R1 + G_2 = -0.000\,2167\,\text{S}$. Then, the parameters $m_0 \approx -1.3661$ and $m_1 \approx -0.1708$, and it corresponds to the regime, when three hidden attractors coexist (a limit cycle and two symmetric chaotic attractors) together with two symmetric stable foci. In Table 2, the relation between parameters of the mathematical and the physical models is presented.

Using the experimental setup shown in Fig. 8b, a study of hidden attractors is carried out. In Fig. 9, the examples of phase portraits in the projection onto the (U_1, U_2)-plane are shown in the oscilloscope screen. The experimental setup parameters are fixed in accordance with the above description. The presented phase portraits are obtained for the same parameter values, only the initial condition of the variable U_1 is changed, while the initial condition for U_2 is set equal to zero. The initial condition for the current I_L can also be set to zero. From the vicinity of the zero saddle-focus equilibrium point, the trajectory converges to one of the symmetric stable foci (see the example in Fig. 9a). With a smooth detuning from the zero saddle-focus, the stable equilibrium mode is replaced by a chaotic attractor; Fig. 9b shows an example of one such attractor. Further changing of the initial condition from zero leads to the basin of attraction of the second symmetric stable equilibrium state (see Fig. 9c). Next, we again observe a hidden chaotic attractor (Fig. 9d), a symmetric partner of the previous one (Fig. 9b). Thus, an accurate selection of the initial conditions allows one to discover two symmetric hidden chaotic attractors. The alternation of domains of stable equilibrium and hidden attractors is in a good agreement with the results of the numerical modeling (see the structure of the basins of attraction in Fig. 5e). The oscilloscope photographs clearly show that there is a switch between the mode on the hidden attractor and the mode corresponding to the stable equilibrium. This feature is related to the fact that the basins of attraction of the obtained hidden attractors are rather small and border on the basins of attraction of the stable foci. Therefore, as a result of the noise influence, we can see a switching from one mode to another. Further moving from zero equilibrium leads to transition to the stable limit cycle of a large amplitude. Figure 9e shows this limit cycle on a scale corresponding to the previous experimental phase portraits, similar to that in Fig. 5c.

Table 2 Comparison of the parameters for physical and mathematical models

Parameter	Mathematical model	Physical model	Min	Max
α	8.41	8.4054	8.3886	8.4222
β	12.23	12.2301	12.1812	12.2790
γ	0.0435	0.0435	0.04328	0.04363
m_0	-1.366	-1.3661	-1.3689	-1.3634
m_1	-0.17	-0.1708	-0.1715	-0.1700

Fig. 9 Photographs of an oscilloscope screen, visualizing hidden chaotic attractors in a radiophysical experiment: The shining dot is the initial condition, **a** the stable equilibrium point; **b** the symmetric hidden chaotic attractor; **c** the stable equilibrium point; **d** the symmetric hidden chaotic attractor; **e**, **f** the external limit cycle. In all 6 photographs, the abscissa is U_1 and the ordinate is U_2. The coordinate scales are 0.2 volts for X-axis and 0.1 volts for Y-axis of the square grid in (**a**)–(**e**); and 0.5 volts for X-axis and 0.2 volts for Y-axis, respectively, in (**f**)
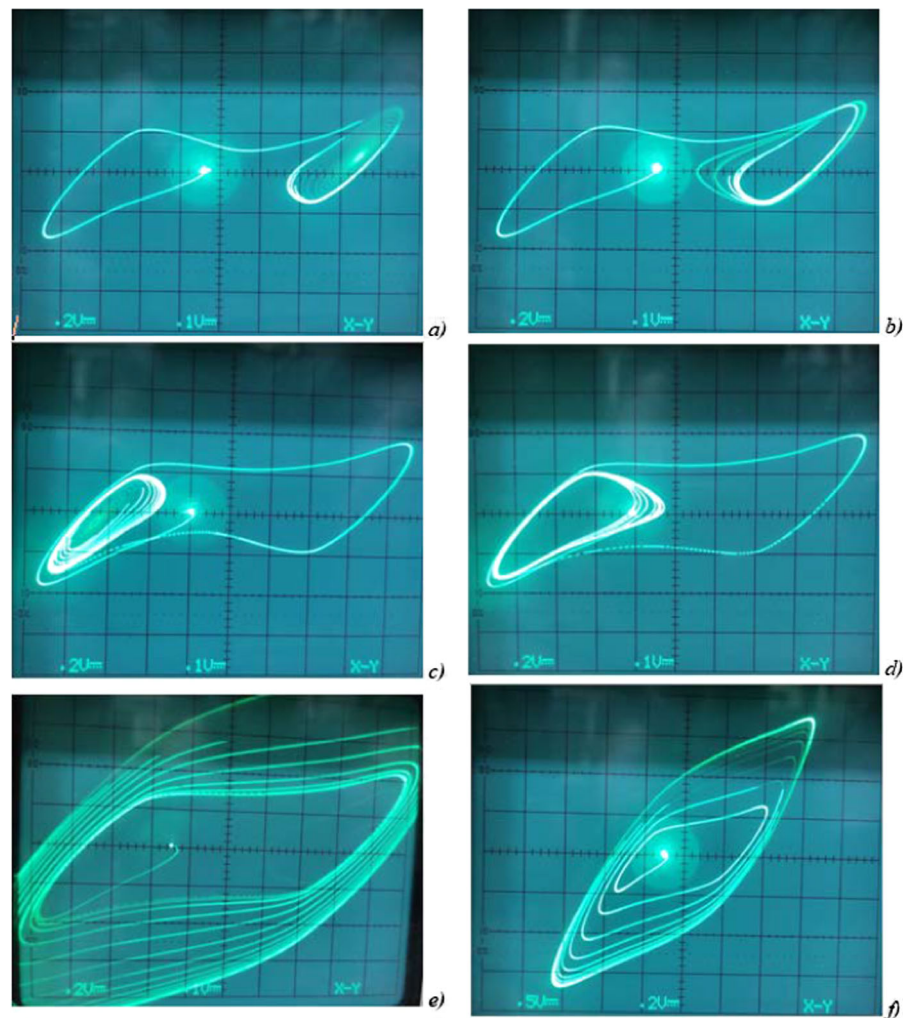
In the experiment, by smoothly changing (selecting) the initial conditions, one can find a saddle limit cycle. In Fig. 9e and f, the initial conditions are chosen near an unstable limit cycle; the trajectory first moves to the unstable limit cycle, performs several oscillations in its vicinity and then tends to the stable limit cycle of a larger amplitude. Note that the invariant

two-dimensional cylinder-shaped stable and unstable manifolds of cycles may play an essential role in partitioning the phase space into basins of attraction (see, e.g., [70–72]).

A comparative analysis of the unstable cycle in the numerical and physical experiments is carried out. Figure 10 shows the time series and two-dimensional pro-

Fig. 10 Visualization of the saddle limit cycle in numerical (**a**) and physical experiments (**b**)
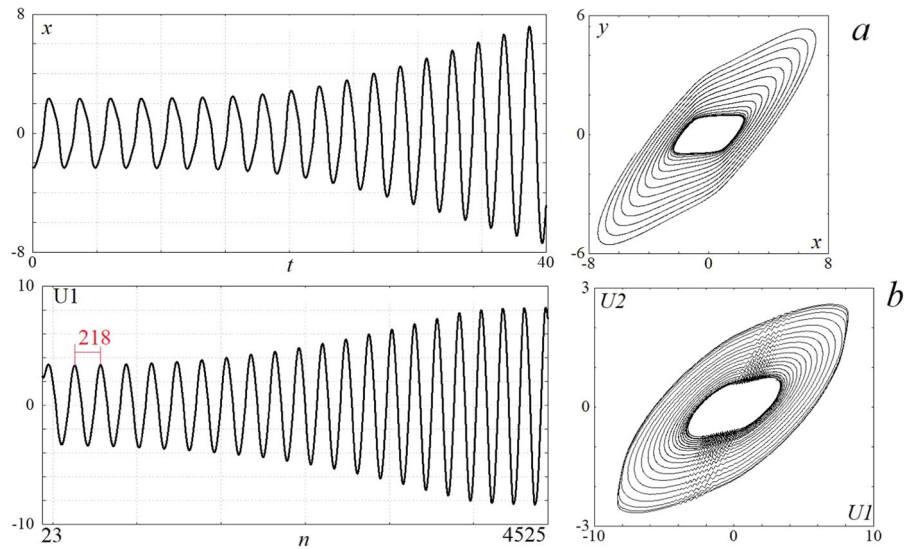
jections of motion of a representative point in the phase space, when choosing initial conditions on the unstable limit cycle. Figure 10a shows the results of numerical calculations, and Fig. 10b shows the data obtained in the physical experiment. In numerical experiment an initial condition on a saddle limit cycle can be obtained by bifurcation analysis packages which then allow to follow the saddle cycle transformation during the change of bifurcation parameter. For our configuration of attractors we cannot find this cycle in depending on the parameter m_1. That is why we found another bifurcation rout in the parameter space leading to occurrence of the saddle cycle (see details in [5]). Then the transformation of saddle cycle along the route is traced to construct the cycle for the desired value of m_1, and we get the following initial condition for the saddle cycle visualization in Fig. 10a: $x_0 = -2.321$, $y_0 = -0.787$, $z_0 = 3.129$. The experimental time series (see Fig. 10b) is constructed for the reference points, the sampling step is $2.5\,\mu$s, respectively, the length of the presented time series is 11.255 m s. Obtaining the model, we renormalize the dynamical variables according to the renormalization factor 1.16, i.e., close to unity; therefore, the amplitudes of oscillations of the numerical model and the experimental implementation are in a good agreement. However, the *time* in model (6) is dimensionless and is normalized to the constant $RC2$. In the numerical simulations, the oscillation period for the unstable cycle is $T_{UC}^{num} = 2.406$. To convert this period to the dimensional form, it is necessary to multiply it by the normalization constant:

$T_{UC}^{num} = 2.406*311*10^{-9}*788 = 0.59$ m s. According to the experimental time series, the oscillation period for the unstable limit cycle is 218 samples, which corresponds to $T_{UC}^{exp} = 0.55$ m s. This is close enough to the values obtained numerically. Table 3 shows a comparison of the parameters of mathematical model (6) and the data obtained in the physical experiment.

An important and interesting feature of comparing the numerical and experimental implementations is the characteristic of the oscillation time on the unstable limit cycle. It is clearly seen that in the numerical experiment, the trajectory makes 11 oscillations in the vicinity of the unstable limit cycle, after that it escapes the vicinity of the cycle. Meanwhile, only 8 oscillations are visible in the physical experiment. This metric can be used as an estimation of the noise in the physical model. In mathematical modeling, the role of noise is played by the numerical errors of the calculation scheme. To construct the trajectory, the fourth-order Runge–Kutta method with a constant integration step equal to 10^{-3} is used. In a physical experiment, the noise voltage consists of several parts: noise of the op-amps, in which the spectral density of the noise voltage at the output is 25nV$/\sqrt{Hz}$; the capacitor's noise is 0.3 mV; external noise and ripple. Also, in the case of absence of voltages at the inputs of op-amps, the output voltage differs from zero, which introduces additional small constant voltages that affect the overall operation of the circuit.

The correspondence between the mathematical model and the experimental laboratory model has some limitations. In a physical experiment, noise is always pre-

sented. There are noises, which are mentioned above, associated with fluctuations of voltages and currents. However, one should also not forget about measurement errors. When developing layouts, researchers rely on nominal electrical values of elements, which can vary within 10%. This error is static and can be eliminated by measuring the real electrical values. Within this work, all electrical values are measured using a multimeter; the capacitance of the capacitors and the inductance of the coil are measured using an LCR-meter of the HM8118 type (see, e.g., [73]). However, there is also a dynamical error associated with the error of the measuring device. This error is significantly less than the static one and is 1% of the nominal value for the multimeter, and 0.1% for the HM8118 meter. For the nominal values we measured, the ranges of the maximum and minimum values of the parameters are calculated taking into account the dynamical error, and they are presented in Table 2. It can be seen that the values of the parameters of mathematical model (6) are inside the relevant intervals indicated in this table.

5 Methods to search for hidden attractors and study of multistability

5.1 The hysteresis loop method

Changing the parameters of the mathematical model and carrying out a parametric bifurcation analysis allow one to obtain some bifurcation mechanisms for the birth of attractors. In the physical experiment, this procedure corresponds to a smooth change of some parameters using a mechanical knob. Changing the parameters in the experiment gives some overall view of its dynamics and characteristic modes. The procedure for scanning the parameter space and detecting the boundaries of regions of different modes in the experiment corresponds to the numerical construction of a chart of dynamical modes with inherited initial conditions, discussed in Sect. 3. Changing the scanning direction makes it possible for some situations to localize the multistability regions in the parameter space. For example, in a simple case of multistability, which arises as a result of the subcritical Andronov–Hopf bifurcation, *hysteresis curves* can be obtained experimentally. If we take the value of a parameter before the Andronov–Hopf bifurcation point, self-oscillations cannot be excited; in the experiment, a stable equilib-

rium state is observed in the phase space. After the loss of stability, the trajectory jumps to a limit cycle, which is a result of the subcritical Andronov–Hopf bifurcation. Having found this cycle, if we now smoothly change the parameter in the opposite direction, the state remains on the cycle even when the equilibrium has already become stable again. Thus, we can find the value of the parameter at which a pair of limit cycles (stable and saddle) is born, coexisting with a stable equilibrium state. Such a loop is commonly referred to as a *hysteresis curve* (see, e.g., [74, p. 643]).

A similar situation can be observed in our case. Figure 11 shows the bifurcation diagram and trees of this type for the considered mathematical model of Chua circuit (6)–(7), which are some analog of the hysteresis curve. Scanning the parameter m_1 interval with decreasing (Fig. 11b), we reach the Andronov–Hopf bifurcation point, where the equilibrium state becomes unstable and the trajectories go to symmetric self-excited chaotic attractors. With further decreasing m_1 symmetric self-excited attractors are merged into one self-excited attractor. If we now start from the region of small values of m_1, where the merged self-excited chaotic attractor exists, and will increase parameter m_1 (Fig. 11c), then we can find an interval, where chaotic attractor dived into symmetric pair and then becomes hidden and coexisting with symmetric stable equilibrium states.

The hysteresis curve provides some overall view into the types of dynamical behavior of the system. However, not in all cases it is possible to detect the full variety of modes in this way. The limitation of the physical characteristics of device in the experiment may not allow going beyond the hysteresis curve and identifying its boundaries; thus, a coexisting attractor may be missed. Also, such configurations of bifurcation diagrams are possible in which the access to hidden attractor by changing the scanning direction of the parameter interval is impossible. A similar situation is possible in the Chua system with the parameters discussed in Sect. 3 (see Fig. 6). In contrast to the case shown in Fig. 11, when the parameter m_1 decreases, the hidden attractor does not transform into a self-excited one: before the bifurcation threshold of the loss of stability of symmetric equilibrium states, the hidden attractor collapses as a result of the crisis. Thus, in this case, scanning the parameter interval does not allow detecting hidden attractors even in numerical experiments with direct integration. It is necessary to choose spe-
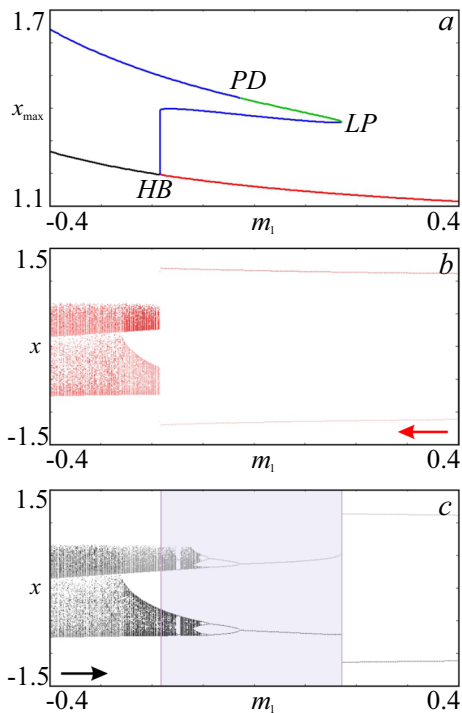
Fig. 11 Bifurcation diagram (**a**) and trees (**b**, **c**) for parameters $\alpha = 8.4$, $\beta = 12.2$, $\gamma = 0.0$, $m_0 = -1.16$. LP is a saddle-node bifurcation; HB is an Andronov–Hopf bifurcation; PD is a period-doubling bifurcation

cial initial conditions leading to the hidden attractor (i.e., in its basin of attraction).

In a physical experiment, the situation is even more complicated since the parameters m_0 and m_1 are determined by seven resistors, some of which defines the values of both parameters. In a simplified form, the dependence of m_0 and m_1 on the values of electrical resistance of resistors is given by Eq. (8). Accordingly, using resistors $R3$ and $R4$, we can independently change the coefficient m_0. Moreover, a change in m_1 necessarily entails a change in m_0. Thus, to select the parameters we need to search for suitable nominal electrical values in a multi-parameter space. The question of accessibility and usability of the entire plane (m_0, m_1) from a physical point of view requires additional attention.

5.2 The advanced harmonic balance method

Now we compare the described results of our experiments with the analytical results of applying the harmonic balance method to the mathematical model of Chua circuit (6).

The *harmonic balance method* (HBM, or describing function method) [75,76] is an approximate method to search for periodic oscillations in nonlinear systems.

Consider a 3-dimensional system in the Lurie form [6]

$$\dot{u} = P u + q \psi(\sigma), \quad \sigma = r^* u, \quad (11)$$

where for Chua system (6)–(7) we have $u = (x, y, z)^*$ and

$$P = \begin{pmatrix} -\alpha(m_1 + 1) & \alpha & 0 \\ 1 & -1 & 1 \\ 0 & -\beta & -\gamma \end{pmatrix}, \quad q = \begin{pmatrix} -\alpha \\ 0 \\ 0 \end{pmatrix}, \quad r = \begin{pmatrix} 1 \\ 0 \\ 0 \end{pmatrix},$$

$$\psi(\sigma) = (m_0 - m_1) \operatorname{sat}(\sigma)$$
$$= \tfrac{1}{2}(m_0 - m_1)(|x+1| - |x-1|). \quad (12)$$

Here operator $*$ denotes transposition operation. For our case $\psi(-\sigma) = -\psi(\sigma)$, the HBM searches for a $2\pi/\omega_0$-periodic solution $u(t) = u(t + 2\pi/\omega_0)$ such that $\sigma(t) = r^* u(t) \approx a_0 + a_1 \cos \omega_0 t$, where a_0 is a shift and $a_1 > 0$ is an amplitude. If the matrix P is non-singular, i.e.,

$$\det P = -\alpha\big((\beta + \gamma)m_1 + \beta\big) \neq 0,$$

and does not have purely imaginary eigenvalues, then we can define the frequency $\omega_0 > 0$ and coefficient of harmonic linearization k such that

$$\operatorname{Im} W_P(i\,\omega_0) = 0, \qquad k = -\big(\operatorname{Re} W_P(i\,\omega_0)\big)^{-1}, \quad (13)$$

otherwise ω_0 is known and $k = 0$. Here, $W_P(s) = r^*(P - s I)^{-1} q$ denotes a *transfer function* of system (11), i.e., a complex-valued function, which is the ratio between the Laplace transforms of the output signal $\sigma(t)$ and of the input signal $\xi(t)$ for the initial state $u(0) = 0$ [77].

Then, we rewrite system (11) as follows:

$$\dot{u} = P_0 u + q \varphi(r^* u), \quad (14)$$

where $\varphi(\sigma) = \psi(\sigma) - k\sigma$, and the matrix $P_0 = P + k q r^*$ has a pair of pure-imaginary eigenvalues $\pm i \omega_0 \neq 0$. The transfer function for system (14) is as follows: $W_{P_0}(s) = r^*(P_0 - s I)^{-1} q$. Following the HBM, the

values $a_{0,1}$ are defined by equations:

$$\frac{2\pi a_0}{\omega_0} + W_{P_0}(0) \int_0^{\frac{2\pi}{\omega_0}} \varphi(a_0 + a_1 \cos(\omega_0 \tau)) \mathrm{d}\tau = 0, \tag{15}$$

$$\Phi(a_0, a_1) = \int_0^{\frac{2\pi}{\omega_0}} \varphi(a_0 + a_1 \cos(\omega_0 \tau)) \cos(\omega_0 \tau) \mathrm{d}\tau = 0,$$

where $\Phi(a_0, a_1)$ is called a *describing function* [77]. If $a_0 = 0$, i.e., there is no shift assumed, the first equation in (15) becomes trivial, since $\varphi(\cdot)$ is odd.

The HBM can be rigorously justified, when a small parameter $\varepsilon > 0$ is introduced in the system, i.e., when the nonlinearity $\varphi(\sigma)$ in (14) is changed by $\varepsilon \varphi(\sigma)$:

$$\dot{u} = P_0 u + \varepsilon q \varphi(r^* u). \tag{16}$$

There is always a nonsingular linear transformation $u = Sv$, defined by matrix S, such that

$$J = S^{-1} P_0 S = \begin{pmatrix} 0 & -\omega_0 & 0 \\ \omega_0 & 0 & 0 \\ 0 & 0 & -d \end{pmatrix}, b = S^{-1} q = \begin{pmatrix} b_1 \\ b_2 \\ b_3 \end{pmatrix}, \tag{17}$$

$$c^* = r^* S = \begin{pmatrix} 1 & 0 & -h \end{pmatrix}.$$

Thus, due to invariance of transfer functions with respect to linear transformations, for system (16) we have

$$W_{P_0}(s) = c^* (J - s I)^{-1} b$$
$$= \frac{-b_1 s + b_2 \omega_0}{s^2 + \omega_0^2} + \frac{b_3 h}{s + d}. \tag{18}$$

Developing the ideas from [46,78] we get

Theorem 1 *If* $d > 0$ *and there exist* a_0 *and* $a_1 > 0$ *satisfying* (15) *such that*

$$b_1 \left. \frac{\partial \Phi(a_0, a)}{\partial a} \right|_{a=a_1} < 0, \tag{19}$$

then, for sufficiently small $\varepsilon > 0$, *system* (16) *has a stable periodic solution in the form*

$$S(v_{01} + a_1 \cos(\omega_0 t), v_{02} + a_1 \sin(\omega_0 t), v_{03})^* + O(\varepsilon) \tag{20}$$

with the period $T = \frac{2\pi}{\omega_0} + O(\varepsilon)$ *and*

$$v_{01} = \varkappa \frac{b_2}{\omega_0}, v_{02} = -\varkappa \frac{b_1}{\omega_0},$$

$$v_{03} = -\varkappa \frac{b_3}{d}, \varkappa = a_0 W_{P_0}^{-1}(0).$$

For the opposite sign in (19), *periodic solution* (20) *is of a saddle type.*

For ω_0 and $a_{0,1}$ defined by (13) and (15) the advanced HBM predicts the existence of periodic solutions in system (11), and these predicted periodic solutions can be visualized by Theorem 1 as

$$u^{\mathrm{HBM}}(t) \approx S(v_{01} + a_1 \cos(\omega_0 t), v_{02} + a_1 \sin(\omega_0 t), v_{03})^*.$$

Trajectories with initial data given by Theorem 1

$$u^{\mathrm{HBM}}(0) \approx S(v_{01} + a_1, v_{02}, v_{03})^* \tag{21}$$

can be used for a numerical search of attractors in system (11). However, a rigorous application of Theorem 1 requires the fulfillment of condition (19) for the visualization of a stable periodic orbit from initial point (21) in system (16) with a sufficiently small $\varepsilon = \varepsilon_0$. Then, the transformation of this initial stable periodic orbit in the phase space while increasing ε from ε_0 up to 1 can be considered in a continuation procedure. For that on each step of the continuation procedure, the initial point for a trajectory to be integrated is chosen as the last point of the trajectory integrated on the previous step. If, while changing from ε_0 to 1, there is no loss of stability bifurcation and the considered trajectory approaches an attractor, then at the end of the procedure an attractor of initial system (11) is localized.

Now let us apply the advanced HBM to study the Chua model. For the transfer function of (12), we have $W_P(s) = \frac{Y(s)}{X(s)}$, where $Y(s) = \alpha(s^2 + (\gamma + 1)s + \beta + \gamma)$ and $X(s) = s^3 + ((m_1 + 1)\alpha + \gamma + 1)s^2 + (((m_1 + 1)\gamma + m_1)\alpha + \beta + \gamma)s + \alpha(m_1(\beta + \gamma) + \beta)$. Here $W_P(0) = \frac{\beta + \gamma}{(\beta + \gamma)m_1 + \beta}$. By (13) for $\omega_0 > 0$ we have

$$\omega_0^2 = \frac{-(\gamma^2 + \alpha - 2\beta + 1)}{2}$$
$$\pm \frac{\sqrt{\gamma^4 - 2(\alpha + 2\beta + 1)\gamma^2 - 8\beta\gamma + (\alpha + 1)^2 - 4\beta}}{2}.$$

From (18) with $P_0 = P + k q r^*$, we get

$$k = \frac{-\alpha(m_1 + m_1\gamma + \gamma) + \omega_0^2 - \gamma - \beta}{\alpha(1 + \gamma)}, \quad d = \frac{\alpha + \omega_0^2 - \beta + 1 + \gamma + \gamma^2}{1 + \gamma},$$

$$h = \frac{\alpha(\gamma + \beta - (1 + \gamma)d + d^2)}{\omega_0^2 + d^2}, \quad b_1 = \frac{\alpha(\gamma + \beta - \omega_0^2 - (1 + \gamma)d)}{\omega_0^2 + d^2}, \tag{22}$$

$$b_2 = \frac{\alpha((1 + \gamma - d)\omega_0^2 + (\gamma + \beta)d)}{\omega_0(\omega_0^2 + d^2)}, \quad b_3 = 1, \quad W_{P_0}(0) = \frac{b_2}{\omega_0} + \frac{h}{d}.$$

From (17), we get the matrix $S = \{s_{ij}\}_{i,j=1}^3$ with

$$s_{11} = 1, \qquad s_{12} = 0, \qquad s_{13} = -h,$$

$$s_{21} = m_1 + 1 + k, \quad s_{22} = -\frac{\omega_0}{\alpha},$$

$$s_{23} = -\frac{h(\alpha(m_1 + 1 + k) - d)}{\alpha},$$

$$s_{31} = \frac{\alpha(m_1+k)-\omega_0^2}{\alpha}, \; s_{32} = -\frac{\alpha(\beta+\gamma)(m_1+k)+\alpha\beta-\gamma\omega_0^2}{\alpha\omega_0},$$
$$s_{33} = h\frac{\alpha(m_1+k)(d-1)+d(1+\alpha-d)}{\alpha}.$$

Computation of the integrals in (15) gives the following:

- if $(-1 < a_0+a_1 \le 1$ and $a_0 \le -1)$ or $(a_0+a_1 \le 1$ and $a_0 > -1$ and $a_0 - a_1 < -1)$, then

$$
\begin{cases}
(m_0-m_1)\Big(-\frac{\pi}{2}(1-a_0) + (1+a_0)\arcsin\frac{1+a_0}{a_1} \\
\quad + \sqrt{a_1^2 - (1+a_0)^2}\Big) = -\frac{\pi a_0}{W_P(0)}, \\
(m_0-m_1)\Big(a_1\big(\frac{\pi}{2} + \arcsin\frac{1+a_0}{a_1}\big) \\
\quad + (1+a_0)\sqrt{1 - \frac{(1+a_0)^2}{a_1^2}}\Big) = \pi a_1 k, \\
\frac{\partial \Phi(a_0,a_1)}{\partial a_1} = \frac{1}{\omega_0}\Big[(m_0-m_1)\Big(\frac{\pi}{2} + \arcsin\frac{1+a_0}{a_1} \\
\quad s - \frac{1+a_0}{a_1}\sqrt{1 - \frac{(1+a_0)^2}{a_1^2}}\Big) - \pi k\Big].
\end{cases}
\tag{23}
$$

- if $(a_0 - a_1 < 1$ or $a_0 \le 1)$ and $a_0 - a_1 \ge -1$ and $(a_0 > 1$ or $a_0 + a_1 > 1)$, then

$$
\begin{cases}
(m_0-m_1)\Big(\frac{\pi}{2}(1+a_0) - (1-a_0)\arcsin\frac{1-a_0}{a_1} \\
\quad - \sqrt{a_1^2 - (1-a_0)^2}\Big) = -\frac{\pi a_0}{W_P(0)}, \\
(m_0-m_1)\Big(a_1\big(\frac{\pi}{2} + \arcsin\frac{1-a_0}{a_1}\big) \\
\quad + (1-a_0)\sqrt{1 - \frac{(1-a_0)^2}{a_1^2}}\Big) = \pi a_1 k, \\
\frac{\partial \Phi(a_0,a_1)}{\partial a_1} = \frac{1}{\omega_0}\Big[(m_0-m_1)\Big(\frac{\pi}{2} + \arcsin\frac{1-a_0}{a_1} \\
\quad - \frac{1-a_0}{a_1}\sqrt{1 - \frac{(1-a_0)^2}{a_1^2}}\Big) - \pi k\Big].
\end{cases}
\tag{24}
$$

- if $(a_0 - a_1 < -1$ and $(a_0 > 1$ or $a_0 + a_1 > 1))$ or $(a_0 \le -1$ and $a_0 + a_1 > 1)$, then

$$
\begin{cases}
(m_0-m_1)\Big((1+a_0)\arcsin\frac{1+a_0}{a_1} - (1-a_0)\arcsin\frac{1-a_0}{a_1} \\
\quad + \sqrt{a_1^2 - (1+a_0)^2} - \sqrt{a_1^2 - (1-a_0)^2}\Big) = -\frac{\pi a_0}{W_P(0)}, \\
(m_0-m_1)\Big(a_1\big(\arcsin\frac{1-a_0}{a_1} + \arcsin\frac{1+a_0}{a_1}\big) \\
\quad + (1-a_0)\sqrt{1 - \frac{(1-a_0)^2}{a_1^2}} + (1+a_0)\sqrt{1 - \frac{(1+a_0)^2}{a_1^2}}\Big) = \pi a_1 k, \\
\frac{\partial \Phi(a_0,a_1)}{\partial a_1} = \frac{1}{\omega_0}\Big[(m_0-m_1)\Big(\arcsin\frac{1-a_0}{a_1} + \arcsin\frac{1+a_0}{a_1} \\
\quad - \frac{1+a_0}{a_1}\sqrt{1 - \frac{(1+a_0)^2}{a_1^2}} - \frac{1-a_0}{a_1}\sqrt{1 - \frac{(1-a_0)^2}{a_1^2}}\Big) - \pi k\Big].
\end{cases}
\tag{25}
$$

Case 1. For Chua system (6)–(7) with the parameters

$$\alpha = 8.4, \; \beta = 12, \gamma = 0, \; m_0 = -0.12,$$
$$m_1 = -1.15 \tag{26}$$

the advanced HBM [see (13), (15), (23)–(25)] predicts the existence of 8 periodic orbits, 2 of which are symmetric and another 6 have shifts with respect to zero equilibrium F_0 (see Fig. 12a):

k	ω_0	a_0	a_1	Thm. 1, Eq. (19)
0.9686	3.2367	± 0.0446	1.2237	Unstable
		0	1.1587	Unstable
0.2123	2.0306	± 3.2148	4.6062	unstable
		± 2.935	4.7771	Stable
		0	6.1492	Stable

For $\omega_0 = 2.0306$, $a_0 = 0$, $a_1 = 6.1492$ (and $T = 3.0941$, $d = 1.5235$), the trajectory with initial data given by (21)

$$x(0) = 6.1492, \; y(0) = 0.3832, \; z(0) = -8.7846 \tag{27}$$

tends to a stable periodic orbit for $\varepsilon = 0.1$. The continuation procedure (with $\varepsilon_0 = 0.1$, increment of ε by 0.3, and integration on time interval [0, 150]) leads to localization of the hidden chaotic Chua attractor $\mathcal{A}_+^{hid}$ in Fig. 12c [46,50]. However, in this case, the basins of attraction of $\mathcal{A}_\pm^{hid}$ contain the initial point given by (21); thus, the attractors can be visualized directly from this point without the continuation procedure (see Fig. 12b). To localize the symmetric attractor $\mathcal{A}_-^{hid}$ one can use symmetry of system (6)–(7).

The trajectories with initial point (21) (i.e., (1.1791, 1.0018, -1.7036) and (1.3915, 0.2871, -3.3656)) on

two predicted stable nonsymmetric periodic orbits for $\varepsilon = 0.1$ tend to the symmetric stable periodic orbit instead of visualizing additional attractors. This shows the significance of smallness of the parameter ε in Theorem 1 and the difference in the initial data for (20) and (21).

Three predicted unstable periodic orbits in vicinity of stable zero equilibrium may be considered as another justification of the *Chua conjecture* stating that the birth of the hidden attractor in the Chua system is connected with the subcritical Andronov–Hopf bifurcation [5].

Case 2. For Chua system (6)–(7) with

$$\alpha = 8.41, \quad \beta = 12.23, \quad \gamma = 0.0435,$$
$$m_0 = -1.366, \quad m_1 = -0.17, \tag{28}$$

the advanced HBM predicts the existence of 6 periodic orbits, 2 of which are symmetric and another 4 have shifts with respect to zero equilibrium F_0 (see Fig. 13a):

k	ω_0	a_0	a_1	Thm. 1, Eq. (19)
-0.0746	3.2392	± 1.4214	0.5447	Unstable
		0	20.3926	Stable
-0.7511	2.1344	± 0.7813	1.0797	Unstable
		0	1.9329	Unstable

The trajectory with initial point

$$x(0) = 20.3926, \quad y(0) = 15.4037, \quad z(0) = -30.4309 \tag{29}$$

on predicted stable periodic orbit ($T = 1.9397, d = 7.396$) visualizes a stable stable periodic orbit in system (16) for $\varepsilon \in (0, 1]$. For $\varepsilon = 1$ this periodic orbit represents a hidden attractor $\mathcal{A}^{\text{hid}}_{\text{limCyc}}$.

Trajectories with the initial point on predicted unstable periodic orbit tend to two symmetric hidden chaotic attractors $\mathcal{A}^{\text{hid}}_{\pm}$ (from the initial points $(1.9329, 0.1525, -2.8275)$ and $(-0.8767, 0.4064, 0.6035)$, see Fig. 13a) and to stable symmetric equilibria $S_{\pm}$.

Case 3. For Chua system (6)–(7) with

$$\alpha = 8.4, \quad \beta = 12.2, \quad \gamma = 0,$$
$$m_0 = -1.16, \quad m_1 = -0.14, \tag{30}$$

the situation is similar to the previous case, and the advanced HBM and predicts the existence of 6 periodic orbits, 2 of which are symmetric and another 4 have shifts with respect to zero equilibrium F_0. The disposition of these periodic orbit is similar to Fig. 13a:

k	ω_0	a_0	a_1	Thm. 1, Eq. (19)
-0.0451	3.2626	± 1.18	0.2194	Unstable
		0	28.7658	Stable
-0.7939	2.0869	± 0.6374	0.8	Unstable
		0	1.5061	Unstable

The trajectory with initial point

$$x(0) = 28.7658, \quad y(0) = 23.4401,$$
$$z(0) = -41.7789 \tag{31}$$

on predicted stable periodic orbit ($T = 1.9258, d = 7.8448$) visualizes a stable stable periodic orbit for $\varepsilon \in (0, 1]$, which is a hidden attractor $\mathcal{A}^{\text{hid}}_{\text{limCyc}}$ for $\varepsilon = 1$.

Trajectories with initial points on predicted unstable periodic orbits tend to two symmetric hidden chaotic attractors $\mathcal{A}^{\text{hid}}_{\pm}$ (from the initial points $(1.5061, 0.0995, -2.1874)$ and $(-0.9607, 0.1787, 0.8615)$) and to stable symmetric equilibria $S_{\pm}$.

Along with the HBM presented in this work and rigorously justified for small parameters ε (see Theorem 1) there are other known attempts [79,80] to apply the classical HBM to Chua system (6) represented in the form of a *jerk system*[10] [81]:

$$\dddot{u} = F(u, \dot{u}, \ddot{u}). \tag{32}$$

Following [79,80], system (6)–(7) could be represented in form (32) with respect to x-variable, i.e.,

$$\dddot{x} + ((m_1 + 1)\alpha + \gamma + 1)\ddot{x} +$$
$$+ (((m_1 + 1)\gamma + m_1)\alpha + \beta + \gamma)\dot{x}$$
$$+ \alpha(m_1(\beta + \gamma) + \beta)x$$
$$= \alpha(\ddot{\psi}(x) + (\gamma + 1)\dot{\psi}(x) + (\beta + \gamma)\psi(x)). \tag{33}$$

Here, one faces the following issue: function $\psi(x)$ in the Chua system is only continuous and not smooth enough to consider the expression in the right-hand side of (33).

To avoid this issue, we can rewrite the Chua system in form (32) with respect to z-variable, i.e.,

$$\dddot{z} + ((m_1 + 1)\alpha + \gamma + 1)\ddot{z} +$$
$$+ (((m_1 + 1)\gamma + m_1)\alpha + \beta + \gamma)\dot{z}$$
$$+ \alpha(m_1(\beta + \gamma) + \beta)z =$$
$$= -\alpha\beta \, \psi\left(\frac{1}{\beta}\ddot{z} + \frac{1+\gamma}{\beta}\dot{z} + \frac{\beta+\gamma}{\beta}z\right). \tag{34}$$

---

[10] In mechanics, *jerk* denotes the third derivative of a position with respect to time.
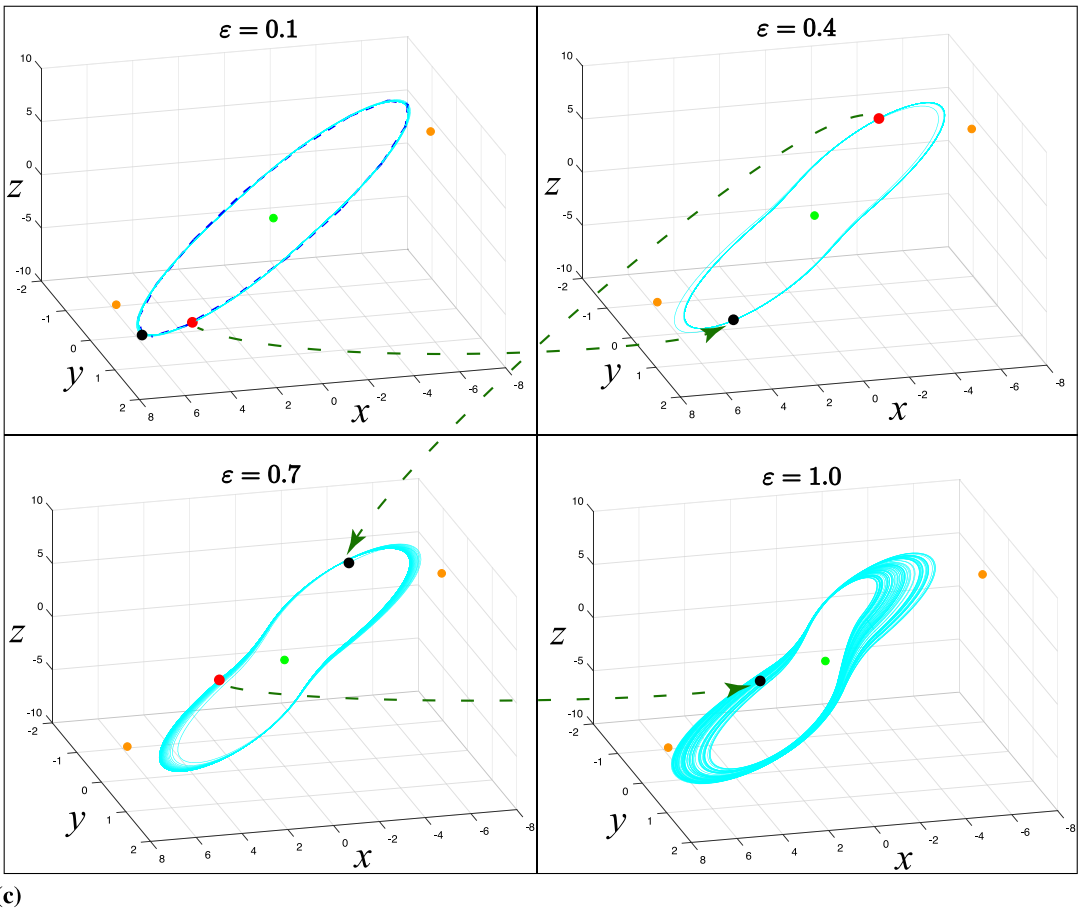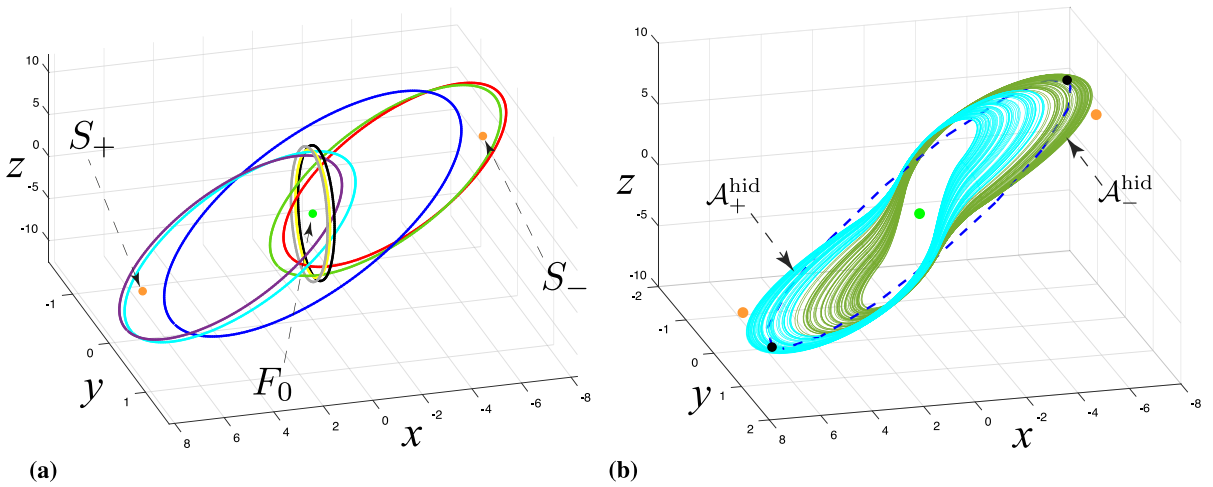
(a)

(b)

(c)

Fig. 12 Initial point $(x(0), y(0), z(0)) = (6.1492, 0.3832, -8.7846)$ (black) on the approximate stable periodic orbit (blue), predicted by HBM, could be used for localization of two hidden chaotic attractors $\mathcal{A}_{\pm}^{\text{hid}}$ (cyan, green) in Chua system (6) with parameters $\alpha = 8.4$, $\beta = 12$, $m_0 = -0.12$, $m_1 = -1.15$
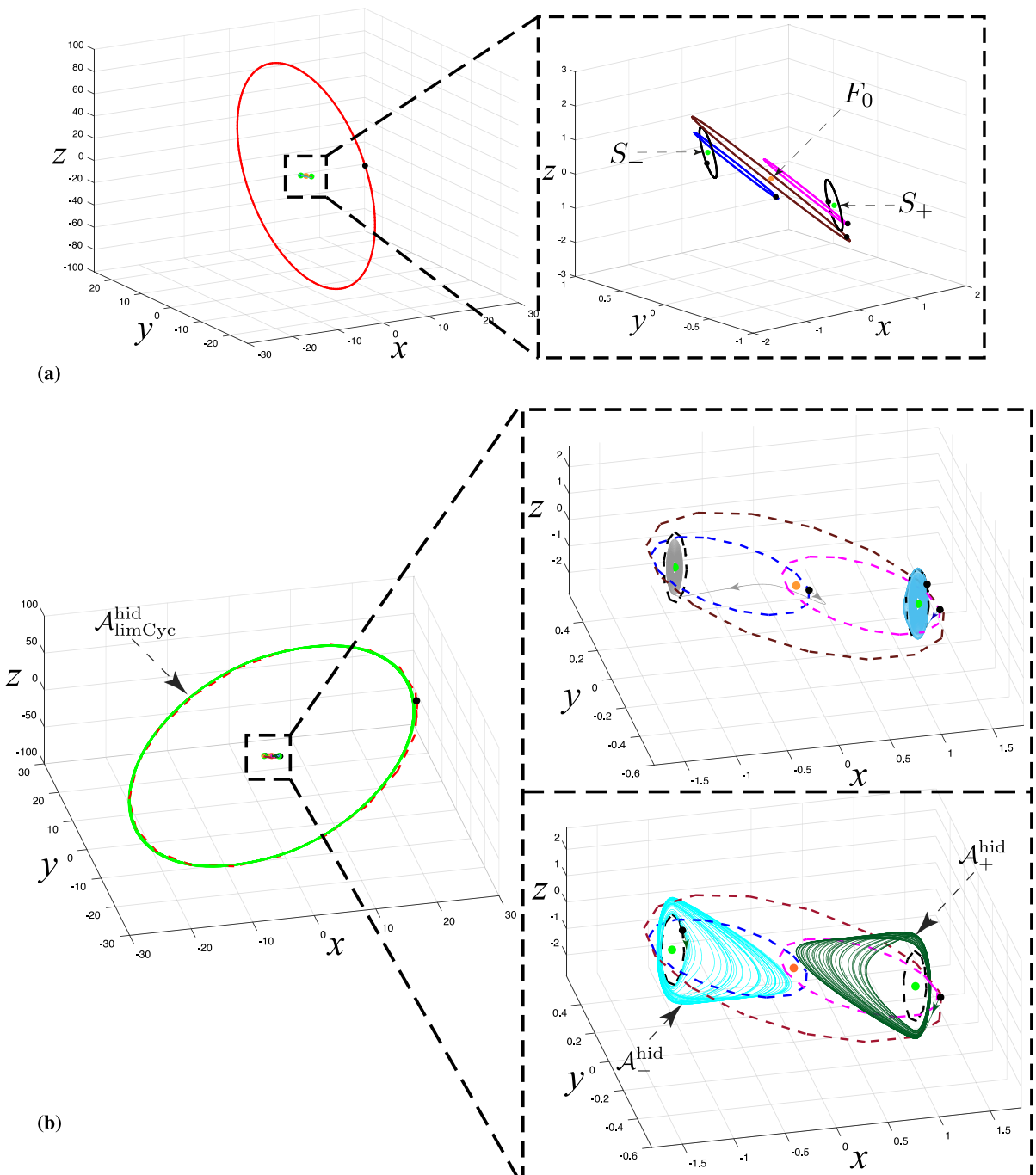
Fig. 13 Initial points on the approximate unstable periodic orbits, predicted by HBM, are used for localization of three hidden attractors ($\mathcal{A}^{\text{hid}}_{\text{limCyc}}$ and $\mathcal{A}^{\text{hid}}_{\pm}$) in Chua system (6) with

$\alpha = 8.41, \beta = 12.23, \gamma = 0.0435, m_0 = -1.366, m_1 = -0.17$. The prediction of unstable periodic orbits could be considered as separation of attractors' basins of attraction

For system (34), the application of the classical HBM [77, p. 450] yields approximate periodic solu-

tions similar to Figs. 12a and 13a, which have the form $z(t) \approx a_0 + a_1 \cos(\omega_0 t)$ and initial data $z(0) = a_0 + a_1$,

$\dot{z}(0) = 0$, and $\ddot{z}(0) = -a_1\omega_0^2$ (but without the additional information about their stability in contrast to Theorem 1).

Visualization and tracking of unstable unstable periodic trajectories, predicted by HBM, due to their instability requires the use of special computational methods (e.g., as in XPPAUT). Here we discuss the possibilities of the Pyragas method for searching and visualizing unstable periodic trajectories (see, e.g., [14,82–85]). The main idea is to construct a control force proportional to the difference between the current state of system (11) and the state delayed by some time in the past:

$$\dot{u} = Pu + q\,\psi(r^*u) + g\,p\left[r^*u(t) - r^*u(t-\tau)\right],$$
(35)

where p is a real vector, $g > 0$ is a feedback gain. If there is a cycle with period T in initial system (11), then for initial condition on this cycle and $\tau = T$ the control is equal zero: $g\,p\left[r^*u(t) - r^*u(t-\tau)\right] \equiv 0$. The coefficient g is chosen so that for initial data not on the cycle the control force the state of the system to tend to the cycle. To tune the parameters g and τ for the search and stabilization of cycles, one can use various adaptive procedures [86–88]. For Chua system (11) using (35) with $p^* = (1, 0, 0)$, $r^* = (1, 0, 0)$, $g = 2.5$ and applying the Pyragas method on time interval $[0, 300]$, starting stabilization from initial point $u_0 = (-2.321, -0.787, 3.129)$ chosen previously in the above numerical experiment (see Sect. 4) we have stabilized an unstable periodic orbit $u^{\text{upo}_1}(t, u_0)$ with period $T \approx 2.4077$ (see Fig. 14), which corresponds to and is in good agreement with the unstable periodic orbit in this physical experiment (see Fig. 10), as well as with the approximate periodic orbit predicted by HMB (see Case 2 and Fig. 13b in Sect. 5.2). The approximate solution from HBM can be used as the initial data for (35). So, for Chua system (11) using same system (35) under control with $g = 2.5$ and applying the Pyragas method on time interval $[0, 700]$, starting stabilization from the orbit approximated by HBM (see Sect. 4) we have stabilized two symmetric unstable periodic orbits $u^{\text{upo}_2}(t, u_0)$ with period $T \approx 1.9566$ embedded into chaotic hidden Chua attractors (see Fig. 15).

Moreover, the Pyragas method and some other powerful methods (see, e.g., [59,89]) allow one to reveal more various periodic orbits embedded into chaotic Chua attractors, which have not been detected above

by the HBM. However, in some cases, the use of the HBM makes it possible to accurately identify all periodic orbits in a system. For example, for the system [90,91]

$$\ddot{x} + x - b\dot{x}\cos(x) = 0$$
(36)

with $b \neq 0$ this method predicts an infinite number of periodic orbits in the form $x^{\text{HBM}}(t) = a_0^i\sin(t)$, where $\{a_0^i\}_{i=1}^{\infty}$ are zeros of the Bessel function: $J_1(a_0^i) = \frac{1}{\pi}\int_0^{\pi}\cos(\tau - a_0^i\sin\tau)d\tau = 0$. True periodic orbits of this system can be visualized from the obtained initial data. For this system approximations of the nonlinearity $\dot{x}\cos(x)$ by its expansion in the Taylor series leads one to the case of the 16th Hilbert problem on the maximum number of coexisting periodic attractors and repellers and their disposition in two-dimensional polynomial systems (which was formulated in 1900 [26] and is still unsolved even for quadratic polynomials [40,46,92,93]). Remark that for this system the similar straightforward application of the XPPAUT package, as above for the Chua system, does not provide initial data for the visualization of all hidden periodic attractors.

6 Conclusion

In this work, a comparative analysis of three Chua's models is carried out, i.e., (1) a mathematical model; (2) a schematic circuit model made of ideal circuit elements; and (3) a physical model of the Chua circuit in the form of a laboratory model made of an interconnection of electronic devices. The developed laboratory model of the experimental setup has an additional sub-circuit included in the classical Chua circuit, which makes it possible to implement the changing of the initial conditions.

In the frame of this work, mathematical modeling of the dynamics of the Chua system is carried out. Bifurcation mechanisms of the appearance of hidden attractors are shown. These mechanisms are associated with some local bifurcation: the subcritical Andronov–Hopf bifurcation, as well as the global saddle-node bifurcation of limit cycles and their development. We also demonstrate that the transition between self-excited and hidden attractors can occur via global bifurcations (e.g., crisis of attractor).

An experimental study of the system dynamics is carried out. The experiment shows the possibility of

Fig. 14 Stabilization of the unstable periodic orbit (red) in Chua system (11) using the Pyragas method: **a** the unstable periodic orbit (red) and its approximation via HBM (dark red, dashed) surrounds 2 hidden chaotic attractors (blue and navy blue); **b** stabilization of the unstable periodic orbit from the initial point $(-2.321, -0.787, 3.129)$ along the time interval $[0, 300]$; **c** evolution of the Pyragas control
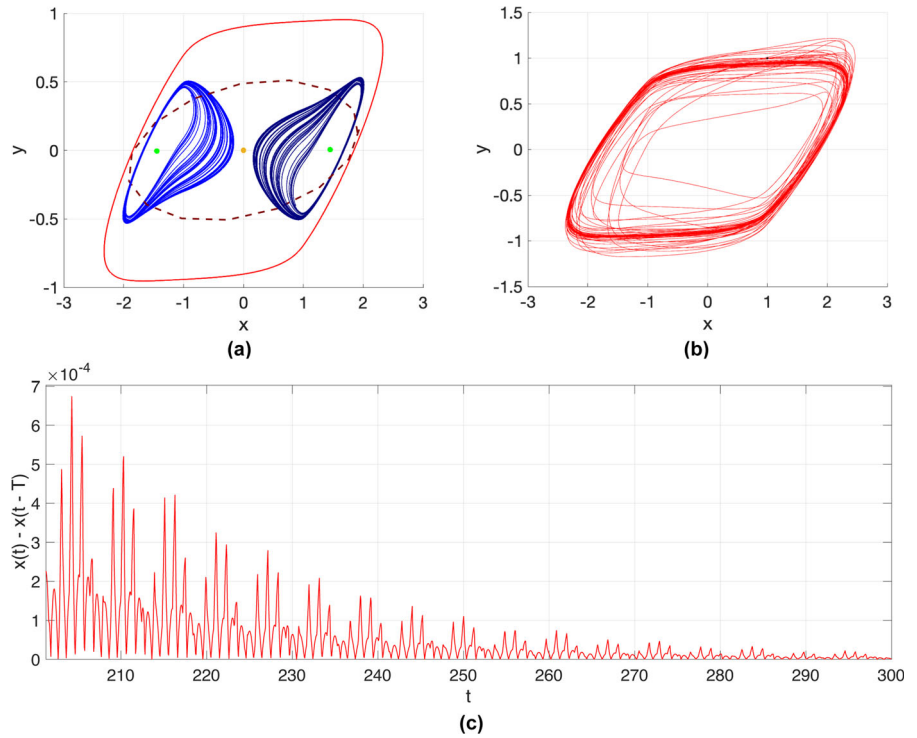

Fig. 15 Stabilization of unstable periodic orbits (red) in Chua system (11) using the Pyragas method: **a** 2 symmetric unstable periodic orbits (red) embedded in 2 hidden chaotic attractors (blue and navy blue) and their approximation via HBM (dark red, dashed); **b** stabilization of the unstable periodic orbit from the orbit approximated by HBM along the time interval $[0, 700]$; **c** evolution of the Pyragas control
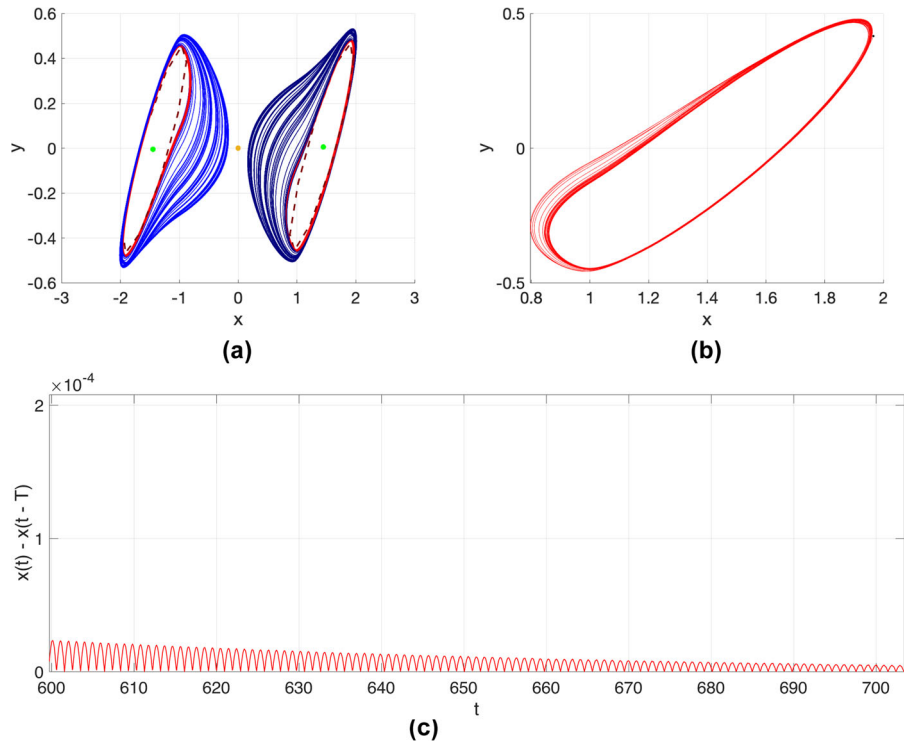
Table 3 Comparison of the parameters for mathematical and physical models for saddle limit cycles

Parameter	Physical model	Mathematical model (direct integration)	Mathematical model (HBM)	Mathematical model (Pyragas method)
Maximal amplitude	3.44	2.350	1.933	2.327
Period, m s	0.55	0.589	0.721	0.590
Period	2.244	2.406	2.944	2.408
Initial point		$(-2.321, -0.787, 3.129)$	$(1.933, 0.152, -2.827)$	$(-2.321, -0.787, 3.129)$

accessing hidden attractors and visualizing of saddle limit cycles. It is shown that in physical experiments where the electronic circuit is triggered by the inclusion of a nonlinear resistor (the Chua diode) in the circuit at zero initial conditions (a starting voltage across the capacitors and the current through the coil), corresponding to zero equilibrium state, only self-excited attractors can be observed. Changing the initial conditions in the experiment allows one to find out hidden attractors. Using this experimental technique for changing initial conditions it is possible to visualize a special class of orbits, i.e., unstable or saddle limit cycles that are rather difficult to detect in a physical experiment. Visualization of such objects is difficult task because we need to find initial conditions on an unstable object. The presence of an accurate mathematical model makes it possible to carry out a numerical bifurcation analysis with the help of which one can trace the bifurcations of not only stable limit cycles, but also the saddle ones, and also visualize them in the phase space. In the experiment, for such visualization one requires special supplements, but even with additional techniques, the trajectories leave such unstable objects much faster and such objects are more difficult to visualize due to the influence of noise. In numerical simulation, the role of noise is played by errors of numerical methods. In this work, it is shown that the noise in the physical experiment is more intense than in the numerical simulations.

Thus, in this work, we used a fairly simple radiophysical generator as an example to show that the detection of coexisting regimes, especially those located far from equilibrium states and having small basins of attraction not connected with equilibria (hidden attractors), may need system modification and development of additional special methods. As demonstrated in this paper the approach based on the existing methods of bifurcation theory and the numerical packages is effec-

tive in studying possible scenarios for the birth of attractors and for the analysis of already discovered attractors (as it happened historically with hidden Chua attractors). However, when solving problems of multistability or global stability, where it is necessary to find all nontrivial attractors or to establish their absence, the key problem of this approach is inability to guarantee the absence of other attractors in the phase space than those found. This is well demonstrated by the famous 16th Hilbert problem on the maximum number of limit cycles of polynomial systems on the plane, where this approach made it possible to construct various nontrivial examples with coexisting limit cycles and obtain a lower estimate of the maximum number of cycles depending on the degree of polynomials on the right side; however, revealing all limit cycles and determining their maximum possible number in the general case remains an unsolved problem. Here analytical methods made it possible to prove that there is only a finite number of limit cycles. If there exist undiscovered limit cycles for some of these examples in the gap between the lower and upper bounds for the maximum number of limit cycles, they will belong to the class of hidden oscillations, since self-excited limit cycles are detected trivially in numerical experiments. Similarly, determining of the exact boundary of global stability in the parameter space, implying the absence of nontrivial attractors in the phase space for given parameters of dissipative system, is difficult, because one needs to analyze hidden parts of the global stability boundary associated with global bifurcations and the birth of hidden attractors. At the same time, conservative (internal) estimates of the boundary of global stability can be obtained using various analytical criteria. The above remains an open question for the Chua system, as well: What is the maximum number of coexisting attractors that can be exhibited in the Chua system and how many of the coexisting attractors can be hidden?

Some additional results on the hidden attractors in the Chua circuits can be found, e.g., in [57,94–105].

Data Availability The data used to support the findings of this study are included within the article.

Declarations

Competing Interests The authors declare that they have no conflict of interest.

References

1. Chua, L., Komuro, M., Matsumoto, T.: The double scroll family. IEEE Trans. Circuits Syst. **CAS–33**(11), 1072 (1986)

2. Chua, L.: A zoo of strange attractors from the canonical Chua's circuits. In: Proceedings of the IEEE 35th Midwest Symposium on Circuits and Systems (Cat. No.92CH3099-9), vol. 2, pp. 916 (1992)

3. Chua, L.: The genesis of Chua's circuit. Arch. Elektron. Übertragungstechnik **42**, 250 (1992)

4. Bilotta, E., Pantano, P.: A Gallery of Chua Attractors. Series A. 61, World Scientific, Singapore (2008)

5. Stankevich, N., Kuznetsov, N., Leonov, G., Chua, L.: Scenario of the birth of hidden attractors in the Chua circuit. Int. J. Bifurc. Chaos Appl. Sci. Eng. **27**(12), 1730038 (2017)

6. Kuznetsov, N.: Theory of hidden oscillations and stability of control systems. J. Comput. Syst. Sci. Int. **59**(5), 647 (2020). https://doi.org/10.1134/S1064230720050093

7. Kuznetsov, N.: Stability and Oscillations of Dynamical Systems: Theory and Applications. PhD thesis, Jyväskylä University Printing House (2008)

8. Leonov, G., Kuznetsov, N.: 4th International Sciecne Conference on Physics and Control (2009). http://www.math.spbu.ru/user/leonov/publications/2009-PhysCon-Leonov-plenary-hidden-oscillations.pdf#page=21

9. Kuznetsov, N., Leonov, G., Vagaitsev, V.: Analytical-numerical method for attractor localization of generalized Chua's system. IFAC Proc. Vol. **43**(11), 29 (2010). https://doi.org/10.3182/20100826-3-TR-4016.00009

10. Leonov, G., Vagaitsev, V., Kuznetsov, N.: Algorithm for localizing Chua attractors based on the harmonic linearization method. Dokl. Math. **82**(1), 663 (2010). https://doi.org/10.1134/S1064562410040411

11. Kuznetsov, N., Neittaanmaki, P.: Open problem on existence of hidden attractor in famous Chua's circuits is solved. CSC News **3–4**, 40 (2015)

12. Kuznetsov, N., Kuznetsova, O., Leonov, G., Vagaytsev, V.: Hidden attractor in Chua's circuits. In: ICINCO 2011—Proceedings of the 8th International Conference on Informatics in Control, Automation and Robotics, vol. 1, p. 279 (2011). https://doi.org/10.5220/0003530702790283

13. Leonov, G., Kuznetsov, N., Vagaitsev, V.: Localization of hidden Chua's attractors. Phys. Lett. A **375**(23), 2230 (2011). https://doi.org/10.1016/j.physleta.2011.04.037

14. Kuznetsov, N., Mokaev, T., Kuznetsova, O., Kudryashova, E.: The Lorenz system: hidden boundary of practical stability and the Lyapunov dimension. Nonlinear Dyn. **102**, 713 (2020). https://doi.org/10.1007/s11071-020-05856-4

15. Kuznetsov, N., Lobachev, M., Yuldashev, M., Yuldashev, R., Kudryashova, E., Kuznetsova, O., Rosenwasser, E., Abramovich, S.: The birth of the global stability theory and the theory of hidden oscillations. In: European Control Conference Proceedings pp. 769–774 (2020). https://doi.org/10.23919/ECC51009.2020.9143726

16. Wang, X., Kuznetsov, N., Chen, G.: Chaotic Systems with Multistability and Hidden Attractors. Springer, Cham (2021)

17. Matsumoto, T.: A chaotic attractor from Chua's circuit. IEEE Trans. Circuits Syst. **31**, 1055 (1984)

18. Zhong, G., Ayrom, F.: Experimental confirmation of chaos from Chua's circuit. Int. J. Circuit Theory Appl. **13**, 93 (1985)

19. Chua, L., Desoer, C., Kuh, E.: Linear and Nonlinear Circuits. McGraw-Hill, New York (1987)

20. Matsumoto, T., Chua, L., Komuro, M.: The double scroll. IEEE Trans. Circuits Syst. **32**(8), 797 (1985)

21. Matsumoto, T., Chua, L., Tokumasu, K.: Double scroll via a two-transistor circuit. IEEE Trans. Circuits Syst. **33**, 828 (1986)

22. Cruz, J., Chua, L.: A CMOS IC nonlinear resistor for Chua's circuit. IEEE Trans. Circuits Syst. I Fundam. Theory Appl. **39**, 985 (1992)

23. Kiliç, R.: A Practical Guide for Studying Chua's Circuits, vol. 71. World Scientific, Singapore (2010)

24. Siderskiy, V.: http://www.chuacircuits.com/howtobuild1.php

25. Chua, L.O., Ayrom, F.: Exploiting the op amp nonlinearity in circuit design. Tech. Rep. UCB/ERL M84/50, EECS Department, University of California, Berkeley (1984). http://www2.eecs.berkeley.edu/Pubs/TechRpts/1984/328.html

26. Hilbert, D.: Mathematical problems. Bull. Am. Math. Soc. **8**, 437 (1902)

27. Dudkowski, D., Jafari, S., Kapitaniak, T., Kuznetsov, N., Leonov, G., Prasad, A.: Hidden attractors in dynamical systems. Phys. Rep. **637**, 1 (2016). https://doi.org/10.1016/j.physrep.2016.05.002

28. Nekorkin, V., Chua, L.: Spatial disorder and wave fronts in a chain of coupled Chua's circuits. Int. J. Bifurc. Chaos **03**(05), 1281 (1993)

29. Kiseleva, M., Kuznetsov, N., Leonov, G.: Hidden attractors in electromechanical systems with and without equilibria. IFAC PapersOnLine **49**(14), 51 (2016). https://doi.org/10.1016/j.ifacol.2016.07.975

30. Leonov, G., Kuznetsov, N., Kiseleva, M., Solovyeva, E., Zaretskiy, A.: Hidden oscillations in mathematical model of drilling system actuated by induction motor with a wound rotor. Nonlinear Dyn. **77**(1–2), 277 (2014). https://doi.org/10.1007/s11071-014-1292-6

31. Leonov, G., Kuznetsov, N., Mokaev, T.: Hidden attractor and homoclinic orbit in Lorenz-like system describing convective fluid motion in rotating cavity. Commun. Nonlinear Sci. Numer. Simul. **28**, 166 (2015). https://doi.org/10.1016/j.cnsns.2015.04.007

32. Leonov, G., Kuznetsov, N., Mokaev, T.: Homoclinic orbits, and self-excited and hidden attractors in a Lorenz-like system describing convective fluid motion. Eur. Phys. J. Spec. Top. **224**(8), 1421 (2015). https://doi.org/10.1140/epjst/e2015-02470-3

33. Sharma, P., Shrimali, M., Prasad, A., Kuznetsov, N., Leonov, G.: Controlling dynamics of hidden attractors. Int. J. Bifurc. Chaos Appl. Sci. Eng. (2015). https://doi.org/10.1142/S0218127415500613

34. Pisarchik, A.N., Feudel, U.: Control of multistability. Phys. Rep. **540**(4), 167 (2014)

35. Best, R., Kuznetsov, N., Leonov, G., Yuldashev, M., Yuldashev, R.: Tutorial on dynamic analysis of the Costas loop. IFAC Annu. Rev. Control **42**, 27 (2016). https://doi.org/10.1016/j.arcontrol.2016.08.003

36. Leonov, G., Kuznetsov, N., Yuldashev, M., Yuldashev, R.: Hold-in, pull-in, and lock-in ranges of PLL circuits: rigorous mathematical definitions and limitations of classical theory. IEEE Trans. Circuits Syst. I Regul. Pap. **62**(10), 2454 (2015). https://doi.org/10.1109/TCSI.2015.2476295

37. Kuznetsov, N., Leonov, G., Yuldashev, M., Yuldashev, R.: Hidden attractors in dynamical models of phase-locked loop circuits: limitations of simulation in MATLAB and SPICE. Commun. Nonlinear Sci. Numer. Simul. **51**, 39 (2017). https://doi.org/10.1016/j.cnsns.2017.03.010

38. Kuznetsov, N., Lobachev, M., Yuldashev, M., Yuldashev, R.: The Egan problem on the pull-in range of type 2 PLLs. Trans. Circuits Syst. II Express Briefs **68**(4), 1467 (2021). https://doi.org/10.1109/TCSII.2020.3038075

39. Kuznetsov, N., Matveev, A., Yuldashev, M., Yuldashev, R.: Nonlinear analysis of charge-pump phase-locked loop: the hold-in and pull-in ranges. IEEE Trans. Circuits Syst. I Regul. Pap. **68**(10), 4049 (2021). https://doi.org/10.1109/TCSI.2021.3101529

40. Arnold, V., Afraimovich, V., Ilyashenko, Y., Shilnikov, L.: Bifurcation Theory and Catastrophe Theory, vol. 5. Springer, Berlin (1994)

41. Ilyashenko, Y., Li, W.: Nonlocal Bifurcations. American Mathematical Society, Rhode Island (1999)

42. Kuznetsov, Y.: Elements of Applied Bifurcation Theory, vol. 112. Springer, Berlin (1998)

43. Andronov, A., Leontovich, E., Gordon, I.I., Maier, A.G.: Theory of Bifurcations of Dynamical Systems on a Plane. Wiley, New York (1973)

44. Afraimovich, V.S., Gonchenko, S.V., Lerman, L.M., Shilnikov, A.L., Turaev, D.V.: Scientific heritage of L.P. Shilnikov. Regul. Chaotic Dyn. **19**(4), 435 (2014)

45. Kuznetsov, N., Reitmann, V.: Attractor Dimension Estimates for Dynamical Systems: Theory and Computation (Dedicated to Gennady Leonov). Springer, Cham (2021)

46. Leonov, G., Kuznetsov, N.: Hidden attractors in dynamical systems. From hidden oscillations in Hilbert–Kolmogorov, Aizerman, and Kalman problems to hidden chaotic attractors in Chua circuits. Int. J. Bifurc. Chaos Appl. Sci. Eng. (2013). https://doi.org/10.1142/S0218127413300024

47. Kuznetsov, N.: The Lyapunov dimension and its estimation via the Leonov method. Phys. Lett. A **380**, 25–26 (2016). https://doi.org/10.1016/j.physleta.2016.04.036

48. Danca, M.F., Kuznetsov, N.: Matlab code for Lyapunov exponents of fractional-order systems. Int. J. Bifurc. Chaos **28**(5), 1850067 (2018). https://doi.org/10.1142/S0218127418500670

49. Kuznetsov, N., Leonov, G., Mokaev, T., Prasad, A., Shrimali, M.: Finite-time Lyapunov dimension and hidden attractor of the Rabinovich system. Nonlinear Dyn. **92**(2), 267 (2018). https://doi.org/10.1007/s11071-018-4054-z

50. Kuznetsov, N., Kuznetsova, O., Leonov, G., Mokaev, T., Stankevich, N.: Hidden attractors localization in Chua circuit via the describing function method. IFAC PapersOnLine **50**(1), 2651 (2017)

51. Rocha, R., Medrano-T, R.O.: Stablity analysis and mapping of multiple dynamics of Chua's circuit in full-four parameter space. Int. J. Bifurc. Chaos **25**, 1530037 (2015)

52. Rocha, R., Medrano-T, R.: Finding hidden oscillations in the operation of nonlinear electronic circuits. Electron.Lett. **52**, 1010 (2016)

53. Leonov, G., Kuznetsov, N., Kudryashova, E.: A direct method for calculating Lyapunov quantities of two-dimensional dynamical systems. Proc. Steklov Inst. Math. **272**(Suppl. 1), S119 (2011). https://doi.org/10.1134/S008154381102009X

54. Ermentrout, B.G.: Simulating, Analyzing, and Animating Dynamical Systems: A Guide to XPPAUT for Researchers and Students. SIAM, Philadelphia (2002)

55. Grebogi, C., Ott, E., Yorke, J.: Chaotic attractors in crisis. Phys. Rev. Lett. **48**(22), 1507 (1982)

56. Stankevich, N., Volkov, E.: Multistability in a three-dimensional oscillator: tori, resonant cycles and chaos. Nonlinear Dyn. **94**(4), 2455 (2018)

57. Menacer, T., Lozi, R., Chua, L.: Hidden bifurcations in the multispiral Chua attractor. Int. J. Bifurc. Chaos **26**(14), 1630039 (2016)

58. Lozi, R., Ushiki, S.: Coexisting chaotic attractors in Chua's circuit. Int. J. Bifurc. Chaos **1**(04), 923 (1991)

59. Ogorzałek, M.J., Galias, Z.: Characterisation of chaos in Chua's oscillator in terms of unstable periodic orbits. J. Circuits Syst. Comput. **3**(02), 411 (1993)

60. Kehlet, B., Logg, A.: A posteriori error analysis of round-off errors in the numerical solution of ordinary differential equations. Numer. Algorithms **76**(1), 191 (2017)

61. Tavazoei, M.S., Haeri, M.: A proof for non existence of periodic solutions in time invariant fractional order systems. Automatica **45**(8), 1886 (2009)

62. Kuznetsov, N., Leonov, G.: Hidden attractors in dynamical systems: systems with no equilibria, multistability and coexisting attractors. In: IFAC Proceedings Volumes, vol. 47, p. 5445. Survey Lecture, 19th IFAC World Congress (2014). https://doi.org/10.3182/20140824-6-ZA-1003.02501

63. Kiseleva, M., Kuznetsov, N., Leonov, G., Neittaanmäki, P.: IEEE 4th International Conference on Nonlinear Science and Complexity, NSC 2012—Proceedings, pp. 109–112 (2012). https://doi.org/10.1109/NSC.2012.6304736

64. Kiseleva, M., Kuznetsov, N., Leonov, G., Neittaanmäki, P.: Discontinuity and Complexity in Nonlinear Physical Systems. vol. 6, chap. Drilling Systems: Stability and Hidden Oscillations. Springer, Berlin (2014). https://doi.org/10.1007/978-3-319-01411-1_15

65. Leonov, G., Kuznetsov, N.: On flutter suppression in the Keldysh model. Dokl. Phys. **63**(9), 366 (2018)

66. Leonov, G., Kuznetsov, N.: On the Keldysh problem of flutter suppression. AIP Conference Proceedings **1959**(1), 020002 (2018). https://doi.org/10.1063/1.5034578

67. Kuznetsov, N.V., Mokaev, T.N., Kudryashova, E.V., Kuznetsova, O.A., Mokaev, R.N., Yuldashev, M.V., Yuldashev, R.V.: in AETA 2018—recent advances. In: Zelinka, I., Brandstetter, P., Trong Dao, T., Hoang Duy, V., Kim, S.B. (eds.) Electrical Engineering And Related Sciences: Theory And Application, pp. 639–644. Springer, Cham (2020)

68. Bezruchko, B., Seleznev, E.: Basins of attraction for chaotic attractors in coupled systems with period doubling. Tech. Phys. Lett. **23**(2), 144 (1997)

69. Datasheet for AD822 op amp. https://pdf1.alldatasheet.com/datasheet-pdf/view/48425/AD/AD822.html

70. Krauskopf, B., Osinga, H.M., Doedel, E.J., Henderson, M.E., Guckenheimer, J., Vladimirsky, A., Dellnitz, M., Junge, O.: A survey of methods for computing (un) stable manifolds of vector fields. Int. J. Bifurc. Chaos **15**(03), 763 (2005)

71. Krauskopf, B., Osinga, H.M.: Numerical Continuation Methods for Dynamical Systems, pp. 117–154. Springer, Berlin (2007)

72. Shilnikov, A., Kolomiets, M.: Methods of the qualitative theory for the Hindmarsh–Rose model: a case study-a tutorial. Int. J. Bifurc. chaos **18**(08), 2141 (2008)

73. Datasheet for HM8118 LCR-Bridge. https://scdn.rohde-schwarz.com/ur/pws/dl_downloads/dl_common_library/dl_brochures_and_datasheets/pdf_1/service_support_30/HM8118_DataSheet_en_03.pdf

74. Andronov, A., Vitt, E., Khaikin, S.: Theory of Oscillators. Pergamon Press, Oxford (1966). [Transl. from Russian: 1937, ONTI NKTP SSSR]

75. Krylov, N., Bogolyubov, N.: Introduction to Non-linear Mechanics. Princeton Univ. Press, Princeton (1947)

76. van der Pol, B.: On relaxation–oscillations. Philos. Mag. J. Sci. **7**(2), 978 (1926)

77. Khalil, H.: Nonlinear Systems. Prentice Hall, Prentice (2002)

78. Leonov, G.: Efficient methods for periodic oscillations search in dynamical systems. App. Math. Mech. **74**(1), 24 (2010)

79. Genesio, R., Tesi, A.: Harmonic balance methods for the analysis of chaotic dynamics in nonlinear systems. Automatica **28**(3), 531 (1992)

80. Genesio, R., Tesi, A.: A harmonic balance approach for chaos prediction: Chua's circuit. Int. J. Bifurc. Chaos **2**(01), 61 (1992)

81. Schot, S.H.: Jerk: the time rate of change of acceleration. Am. J. Phys. **46**(11), 1090 (1978)

82. Pyragas, K.: Continuous control of chaos by self-controlling feedback. Phys. Lett. A **170**(6), 421 (1992)

83. Celka, P.: Experimental verification of Pyragas's chaos control method applied to Chua's circuit. Int. J. Bifurc. Chaos **4**(06), 1703 (1994)

84. Kuznetsov, N., Mokaev, T., Kudryashova, E., Kuznetsova, O., Danca, M.F.: On lower-bound estimates of the Lyapunov dimension and topological entropy for the Rossler systems. IFAC PapersOnLine **52**(18), 97 (2019)

85. Alexeeva, T., Barnett, W., Kuznetsov, N., Mokaev, T.: Time-delay control for stabilization of the Shapovalov mid-size firm model. IFAC PapersOnLine **53**(2), 16971B – 16976 (2020)

86. Lin, W., Ma, H., Feng, J., Chen, G.: Locating unstable periodic orbits: when adaptation integrates into delayed feedback control. Phys. Rev. E **82**(4), 046214 (2010)

87. Lehnert, J., Hövel, P., Flunkert, V., Guzenko, P., Fradkov, A., Schöll, E.: Adaptive tuning of feedback gain in time-delayed feedback control. Chaos Interdiscip. J. Nonlinear Sci. **21**(4), 043111 (2011)

88. Pyragas, V., Pyragas, K.: Adaptive modification of the delayed feedback control algorithm with a continuously varying time delay. Phys. Lett. A **375**(44), 3866 (2011)

89. Ogorzałek, M.J., Galias, Z.: Chua's Circuit: A Paradigm For Chaos, pp. 230–248. World Scientific, Singapore (1993)

90. Kahn, P., Zarmi, Y.: Nonlinear Dynamics. Exploration Through Normal Forms, Wiley, New York (1998)

91. Sprott, J., Jafari, S., Khalaf, A., Kapitaniak, T.: Megastability: Coexistence of a countable infinity of nested attractors in a periodically-forced oscillator with spatially-periodic damping. Eur. Phys. J. Spec. Top. **226**(9), 1979 (2017)

92. Leonov, G., Kuznetsov, N., Kudryashova, E., Kuznetsova, O.: Modern symbolic computation methods: Lyapunov

quantities and 16th Hilbert problem. SPIIRAS Proc. **1**(16), 5 (2011)

93. Kuznetsov, N., Kuznetsova, O., Leonov, G.: Visualization of four normal size limit cycles in two-dimensional polynomial quadratic system. Differ. Equ. Dyn. Syst. **21**(1–2), 29 (2013). https://doi.org/10.1007/s12591-012-0118-6

94. Leonov, G., Kuznetsov, N., Vagaitsev, V.: Hidden attractor in smooth Chua systems. Physica D Nonlinear Phenom. **241**(18), 1482 (2012). https://doi.org/10.1016/j.physd.2012.05.016

95. Li, Q., Zeng, H., Yang, X.S.: On hidden twin attractors and bifurcation in the Chua's circuit. Nonlinear Dyn. **77**(1–2), 255 (2014)

96. Chen, M., Li, M., Yu, Q., Bao, B., Xu, Q., Wang, J.: Dynamics of self-excited attractors and hidden attractors in generalized memristor-based Chua's circuit. Nonlinear Dyn. **81**, 215 (2015)

97. Bao, B., Hu, F., Chen, M., Xu, Q., Yu, Y.: Self-excited and hidden attractors found simultaneously in a modified Chua's circuit. Int. J. Bifurc. Chaos **25**(05), 1550075 (2015). https://doi.org/10.1142/S0218127415500753

98. Chen, M., Yu, J., Bao, B.C.: Finding hidden attractors in improved memristor-based Chua's circuit. Electron. Lett. **51**, 462 (2015)

99. Semenov, V., Korneev, I., Arinushkin, P., Strelkova, G., Vadivasova, T., Anishchenko, V.: Numerical and experimental studies of attractors in memristor-based Chua's oscillator with a line of equilibria, Noise-induced effects. Eur. Phys. J. Spec. Top. **224**(8), 1553 (2015)

100. Chen, M., Yu, J., Bao, B.C.: Hidden dynamics and multistability in an improved third-order Chua's circuit. J. Eng. (2015). https://doi.org/10.1049/joe.2015.0149

101. Zelinka, I.: Evolutionary identification of hidden chaotic attractors. Eng. Appl. Artif. Intell. **50**, 159 (2016)

102. Rocha, R., Ruthiramoorthy, J., Kathamuthu, T.: Memristive oscillator based on Chua's circuit: stability analysis and hidden dynamics. Nonlinear Dyn. **88**(4), 2577 (2017)

103. Zhao, H., Lin, Y., Dai, Y.: Hopf bifurcation and hidden attractor of a modified Chua's equation. Nonlinear Dyn. (2017). https://doi.org/10.1007/s11071-017-3777-6

104. Kiseleva, M., Kudryashova, E., Kuznetsov, N., Kuznetsova, O., Leonov, G., Yuldashev, M., Yuldashev, R.: Hidden and self-excited attractors in Chua circuit: synchronization and SPICE simulation. Int. J. Parallel Emerg. Distrib. Syst. **33**(5), 513 (2018). https://doi.org/10.1080/17445760.2017.1334776

105. Wang, N., Zhang, G., Kuznetsov, N., Bao, H.: Hidden attractors and multistability in a modified Chua's circuit. Commun. Nonlinear Sci. Numer. Simul. **92**, 105494 (2021)